

# Synaptic input and Ca<sup>2+</sup> activity in zebrafish oligodendrocyte precursor cells contribute to myelin sheath formation

Received: 25 March 2022

Accepted: 13 December 2023

Published online: 12 January 2024

 Check for updates

Jiaxing Li <sup>1</sup>, Tania G. Miramontes<sup>1</sup>, Tim Czopka <sup>2</sup> & Kelly R. Monk <sup>1</sup> ✉

In the nervous system, only one type of neuron–glial synapse is known to exist: that between neurons and oligodendrocyte precursor cells (OPCs), yet their composition, assembly, downstream signaling and in vivo functions remain largely unclear. Here, we address these questions using in vivo microscopy in zebrafish spinal cord and identify postsynaptic molecules PSD-95 and gephyrin in OPCs. The puncta containing these molecules in OPCs increase during early development and decrease upon OPC differentiation. These puncta are highly dynamic and frequently assemble at 'hotspots'. Gephyrin hotspots and synapse-associated Ca<sup>2+</sup> activity in OPCs predict where a subset of myelin sheaths forms in differentiated oligodendrocytes. Further analyses reveal that spontaneous synaptic release is integral to OPC Ca<sup>2+</sup> activity, while evoked synaptic release contributes only in early development. Finally, disruption of the synaptic genes *dlg4a/dlg4b*, *gphnb* and *nlg3b* impairs OPC differentiation and myelination. Together, we propose that neuron–OPC synapses are dynamically assembled and can predetermine myelination patterns through Ca<sup>2+</sup> signaling.

OPCs are a dynamic cell type in the CNS that can migrate, proliferate, dramatically remodel processes and differentiate into myelinating oligodendrocytes. OPCs and their interactions with neurons play important roles in CNS health and disease such as myelination and remyelination<sup>1</sup>, neural network remodeling<sup>2</sup> and glioma progression<sup>3</sup>. Synapses form between neurons (presynaptic) and OPCs (postsynaptic) and represent the only known type of glial synapse in the nervous system. The composition of neuron–OPC synapses is largely unknown, except for some synaptic receptors (for example, glutamatergic and GABAergic) that were revealed by pharmacology and electrophysiology<sup>4</sup>. Neuron–OPC synapse assembly and regulation in vivo are mysterious, due in part to a paucity of tools to label these structures. Previous studies knocking down single synaptic receptor types found diverse and sometimes conflicting effects on OPC development and myelination; for example, blocking NMDA receptors reduced or had no effect on myelination<sup>5,6</sup>, and blocking GABA receptors enhanced or had no

effect on OPC proliferation<sup>7,8</sup>. This is possibly due to redundancy, as OPCs possess multiple synaptic receptors<sup>4</sup>. Currently, our understanding of the functions of neuron–OPC synapses is incomplete.

OPCs are hypothesized to sense the activity of neurons through neuron–OPC synapses. Several studies support this idea: neuronal activity can modulate OPC development and myelination<sup>9–13</sup>; axonal stimulation in ex vivo rodent studies was reported to cause synapse-dependent Ca<sup>2+</sup> increases in oligodendrocyte lineage cells, mostly in somas<sup>14–16</sup>. However, the in vivo relationship between neuronal activity, neuron–OPC synapses and OPC Ca<sup>2+</sup> activity without exogenous stimulation is unknown. Furthermore, the role of synapses in forming microdomain (MD) Ca<sup>2+</sup> events in OPC processes<sup>17,18</sup> has not been addressed.

Here we identify postsynaptic scaffold proteins membrane-associated guanylate kinases (MAGUKs) and gephyrin in zebrafish OPCs. The postsynaptic puncta number in OPCs increases during

<sup>1</sup>Vollum Institute, Oregon Health & Science University, Portland, OR, USA. <sup>2</sup>Centre for Clinical Brain Sciences, University of Edinburgh, Edinburgh, UK.

✉e-mail: [g.absent@gmail.com](mailto:g.absent@gmail.com); [monk@ohsu.edu](mailto:monk@ohsu.edu)

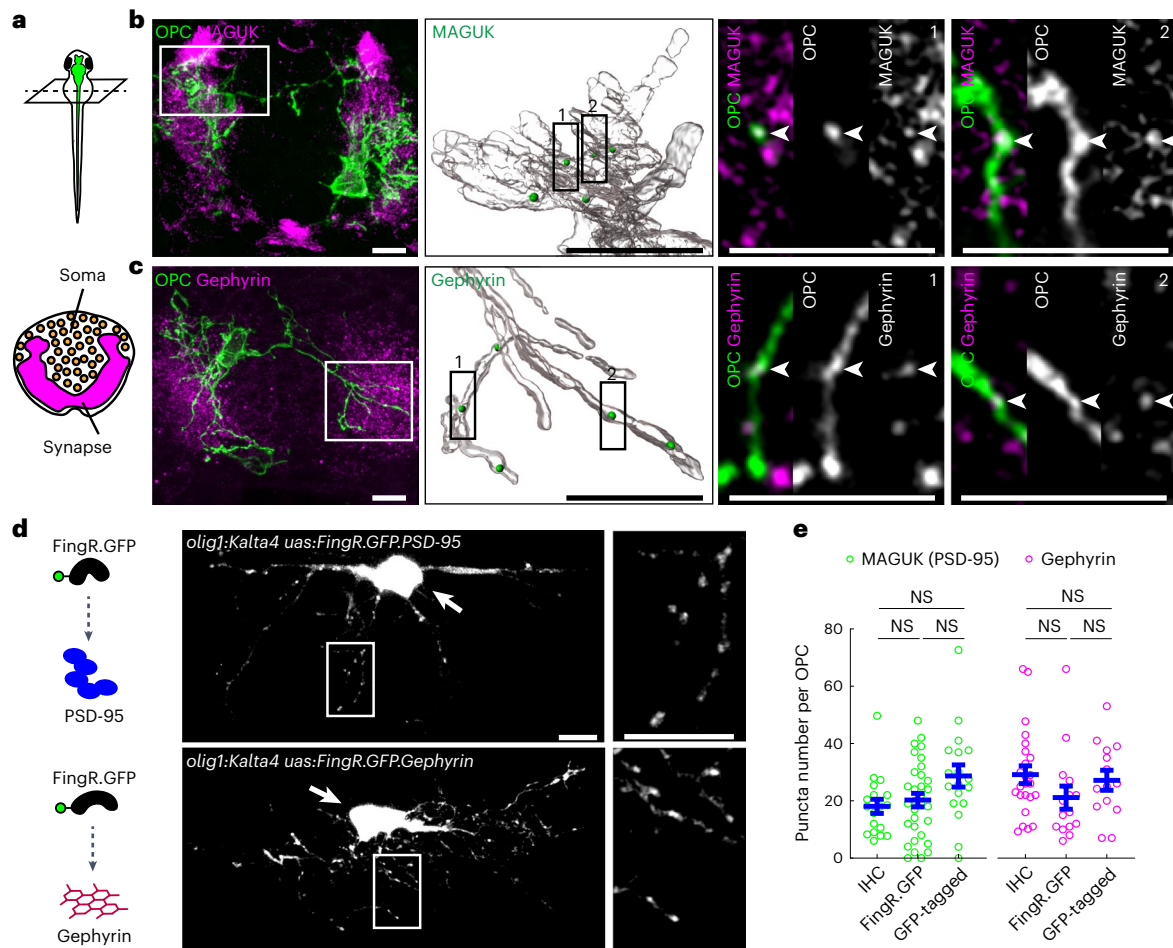


**Fig. 1 | Postsynaptic organizers MAGUK/PSD-95 and gephyrin are present in zebrafish spinal cord OPCs.** **a**, Top, schematic fish model showing transverse section orientation; bottom, distribution of soma and synapses in spinal cord transverse sections. **b,c**, Representative IHC images of MAGUK (**b**) and gephyrin (**c**) in *Tg(olig1:Kalta4,10xUAS:myrGFP)* spinal cord at 3 d.p.f. From left, spinal cord sections, 3D-reconstructed regions, and two examples of puncta in OPCs at single planes. Only the postsynaptic puncta that fall within OPC process volumes are shown in 3D-reconstructed images (green spheres) and are indicated with arrowheads in examples. In each example, from left are the merged channels, the OPC channel, and the MAGUK/gephyrin channel. **d**, Representative images and

enlarged regions of FingR.GFP.PSD-95 and FingR.GFP.gephyrin driven by the *olig1* promoter in OPCs. OPC somas are indicated with arrows. The process regions are enlarged in the right images. The schematic on the left shows FingR.GFP binding to the proteins of interest. **e**, Quantification of puncta number per OPC by IHC (MAGUK and gephyrin), FingR.GFP (PSD-95 and gephyrin) and GFP-tagged (PSD-95 and gephyrin) in the spinal cord. From left,  $n = 18, 32, 18, 24, 15$  and 14 cells from at least 10 fish in each condition. All data are represented as the mean  $\pm$  s.e.m.; NS, not significant; Kruskal–Wallis test followed by Dunn’s multiple-comparison test (**e**); scale bars, 5  $\mu$ m.

early development, reduces upon OPC differentiation and exhibits small differences across CNS regions but no differences between OPC subgroups. In vivo imaging of PSD-95–GFP (a MAGUK member) and GFP–gephyrin puncta in OPCs reveals that the puncta are highly dynamic, presumably resulting in extensive synaptic coverage. Although dynamic, postsynaptic puncta repeatedly assemble at approximately ten hotspots for each OPC. GFP–gephyrin hotspots at the OPC stage predict where a subset of myelin sheaths form at the oligodendrocyte stage, in a synaptic release-dependent manner. Further analysis reveals that  $Ca^{2+}$  activity is associated with neuron–OPC synapses and similarly predicts where myelin sheaths form. The majority of in vivo OPC  $Ca^{2+}$  events occur in MDs, require spontaneous synaptic release, and, during early development, require evoked synaptic release from neurons. Finally, we find that disruption of synaptic genes, *dlg4a* and *dlg4b* (discs large 4a and 4b), *gphnb* (gephyrin b) and *nlg3b* (neuroligin 3b) impairs OPC development and myelination. Collectively, these results suggest that neuron–OPC synapses partially predetermine myelination patterns through preferential assembly and  $Ca^{2+}$  signaling.

## Results

### MAGUK/PSD-95 and gephyrin are present in zebrafish OPCs

Transcript expression of *Dlg4* (encoding PSD-95, often associated with excitatory glutamate receptors) and *gephyrin* (often associated with inhibitory GABA and glycine receptors) were previously reported in zebrafish and mammalian OPCs (Extended Data Fig. 1a,b)<sup>17,19</sup>. We detected the presence of MAGUK/PSD-95 and gephyrin puncta in zebrafish spinal cord OPCs using immunohistochemistry (IHC) at 3 days post-fertilization (d.p.f.; Fig. 1a–c and Extended Data Fig. 1c) and found that puncta were localized to OPC processes and somas (Extended Data Fig. 1d). Next, we visualized postsynaptic puncta using fibronectin intrabodies generated by mRNA display (FingRs) that bind to endogenous PSD-95 and gephyrin in vivo<sup>20</sup>. We found FingR.GFP enrichment in somas (Fig. 1d), similarly to previous reports in neurons<sup>20–22</sup>. More importantly, we observed puncta labeling in OPC processes (Fig. 1d), indicating potential synaptic locations. By IHC and FingRs, we identified  $18.2 \pm 2.5$  and  $20.3 \pm 2.4$  MAGUK/PSD-95 puncta, respectively, and  $29.1 \pm 3.1$  and  $21.1 \pm 4.0$  gephyrin puncta, respectively, for each OPC at 3 d.p.f. (Fig. 1e). Similar results

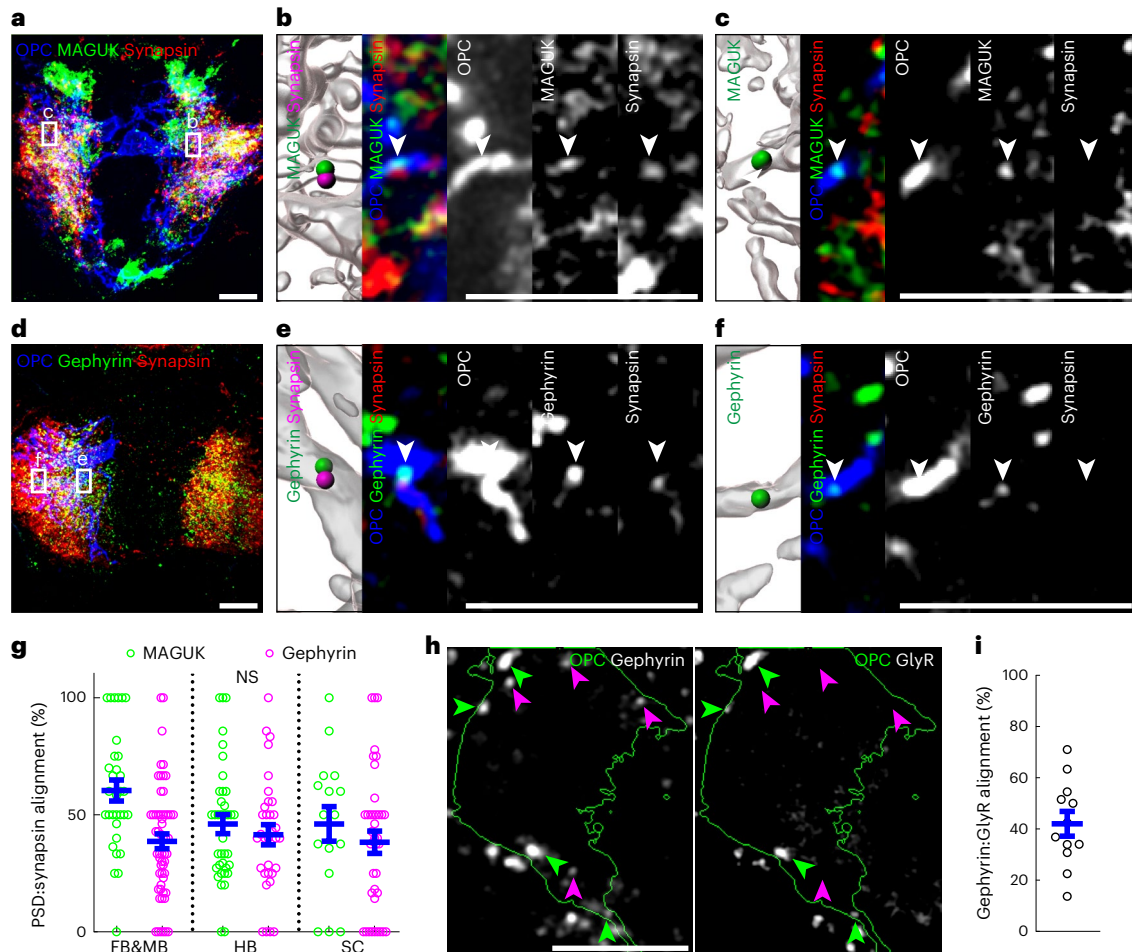


**Fig. 2 | Some but not all MAGUK and gephyrin puncta in OPCs are associated with other synaptic molecules. a–f**, Representative transverse IHC images of MAGUK (**a–c**) and gephyrin (**d–f**) with synapsin in *Tg(olig1:Kalta4,10xUAS:myrGFP)* spinal cord OPCs at 3 d.p.f. Spinal cord sections (**a** and **d**), alignment example with synapsin (**b** and **e**) and no-alignment example with synapsin (**c** and **f**). In each example, from the left are 3D-reconstructed regions, the merged channels, the OPC channel, the MAGUK/gephyrin channel, and the synapsin channel. Only the postsynaptic puncta that fall within OPC process volumes are shown in 3D-reconstructed images (green spheres) with aligned synapsin (magenta spheres) and are indicated with arrowheads in other channels. **g**, The percentage

of MAGUK and gephyrin puncta in an OPC that align with presynaptic synapsin in different CNS regions at 3 d.p.f. FB&MB, forebrain and midbrain; HB, hindbrain; SC, spinal cord. From left,  $n = 32, 57, 38, 33, 16$  and  $39$  cells from at least 10 fish in each condition. **h**, Representative IHC images of gephyrin and glycine receptors (GlyR) in *Tg(olig1:Kalta4,10xUAS:myrGFP)* spinal cord OPCs at 3 d.p.f. OPC boundaries are indicated in green. Gephyrin puncta either align with GlyR (green arrowheads) or do not align with GlyR (magenta arrowheads). **i**, The percentage of gephyrin puncta in an OPC that align with GlyR in spinal cord at 3 d.p.f.  $n = 12$  cells from 7 fish. All data are represented as the mean  $\pm$  s.e.m.; Kruskal–Wallis test followed by Dunn’s multiple-comparison test (**g**); scale bars,  $5 \mu\text{m}$ .

from two distinct methods support the presence of postsynaptic puncta in OPCs and extend previous work that reported PSD-95 in myelin sheaths<sup>23</sup>.

Given that OPCs are heterogeneous according to transcriptomic and electrophysiological studies<sup>24,25</sup>, we examined the number of postsynaptic puncta across developmental stages and CNS regions using IHC. We observed an increasing trend through development: both MAGUK and gephyrin puncta numbers increased from 2 d.p.f. ( $10.4 \pm 1.8$  MAGUK;  $15.9 \pm 2.1$  gephyrin) to 5 d.p.f. ( $28.8 \pm 8.6$  MAGUK;  $68.2 \pm 6.7$  gephyrin; Extended Data Fig. 2a). The postsynaptic puncta numbers per cell were overall similar across CNS regions, except that gephyrin puncta numbers were higher in the forebrain and midbrain ( $20.2 \pm 1.2$ ) compared to the spinal cord ( $13.8 \pm 0.9$ ; Extended Data Fig. 2b), possibly suggesting a preference of OPCs to form synapses with inhibitory neurons in the brain. Within the zebrafish spinal cord, OPC subgroups were previously reported to reside in neuron-rich versus axon-rich and synapse-rich regions (Extended Data Fig. 2c)<sup>17</sup>. We found that postsynaptic puncta numbers were similar between these OPC subgroups (Extended Data Fig. 2d).

### MAGUK and gephyrin in OPCs can align with synaptic molecules

Next, we tested whether these puncta align with presynaptic structures. Using the pan-presynaptic marker synapsin (Fig. 2a–f), we identified MAGUK and gephyrin puncta in OPCs that aligned (Fig. 2b,e) or that did not align (Fig. 2c,f) with synapsin. Around  $46.1\% \pm 7.4\%$  and  $38.3\% \pm 4.8\%$  of MAGUK and gephyrin puncta in an OPC, respectively, aligned with synapsin in the spinal cord, and a similar percentage of puncta in an OPC aligned with synapsin in other CNS regions (Fig. 2g). In addition, at 3 d.p.f.,  $42.1\% \pm 4.8\%$  of gephyrin puncta in an OPC aligned with glycine receptors (Fig. 2h,i). We noted that postsynaptic markers in individual OPCs exhibited a wide range of alignment with presynaptic molecules (0–100%). Altogether, the alignment of MAGUK and gephyrin puncta with other synaptic molecules varies from OPC to OPC, and averages 40–60% throughout the CNS.

### PSD-95–GFP and GFP–gephyrin decrease upon OPC differentiation

To understand synapse assembly and disassembly in OPCs, we conducted *in vivo* time-lapse imaging. We found that FingR.GFP tools were

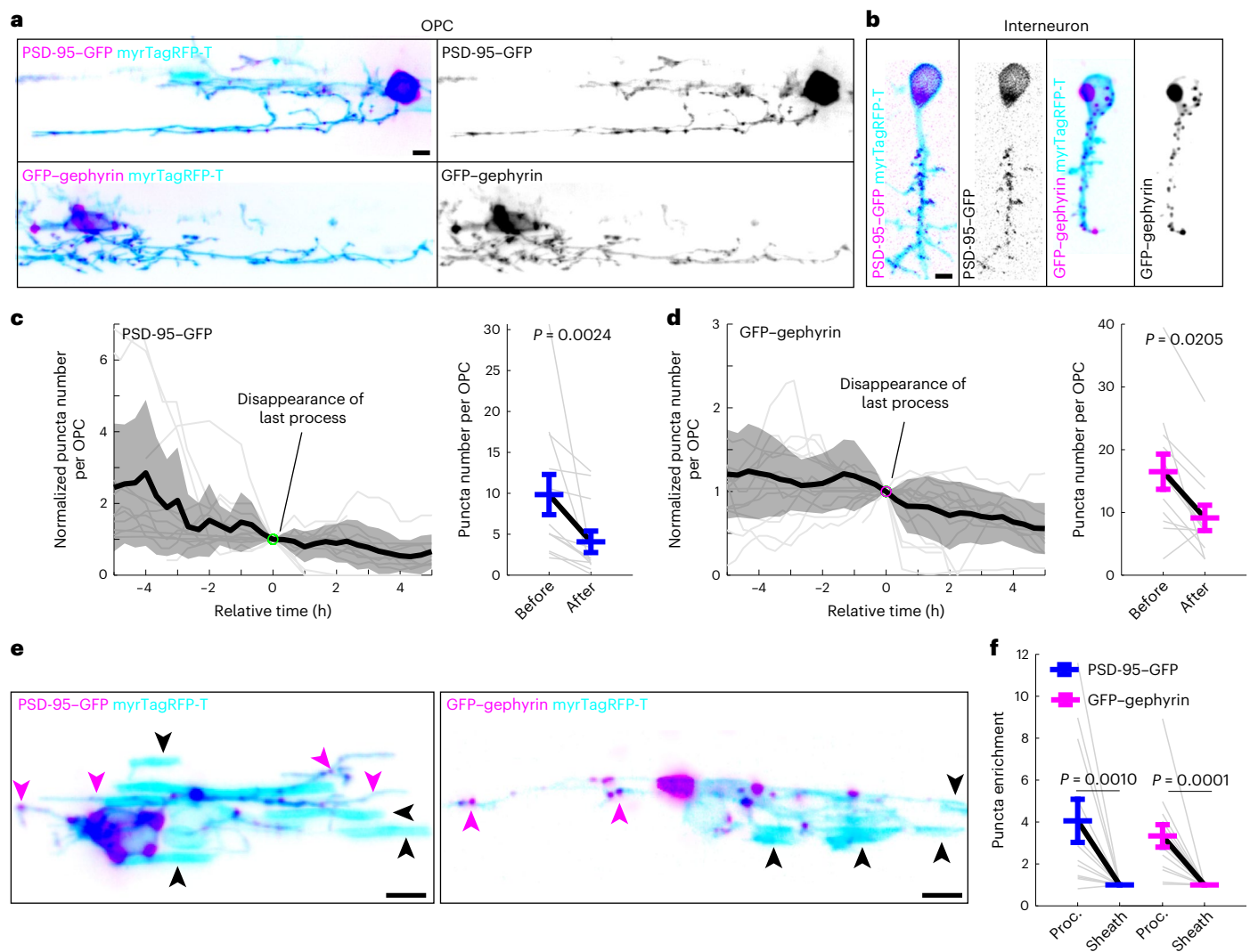


**Fig. 3** **In vivo** imaging reveals downregulation of PSD-95-GFP and GFP-gephyrin upon OPC differentiation. **a,b**, Representative images of PSD-95-GFP and GFP-gephyrin (magenta) in spinal cord OPCs (**a**) and neurons (**b**) at 3 d.p.f. Cell membranes are indicated in cyan. **c,d**, Quantification of PSD-95-GFP (**c**) and GFP-gephyrin (**d**) puncta number in OPCs before and after the last process disappearance, set as time zero, during differentiation. Left, individual traces (gray lines) with the average (black line) and the s.d. (shade). Right, paired comparison before and after time zero. **c**,  $n = 12$  cells from 8 fish;  $t[11] = 3.922$ .

**d**,  $n = 12$  cells from 8 fish;  $t[11] = 2.705$ . **e**, Representative images of PSD-95-GFP and GFP-gephyrin (magenta) in differentiating oligodendrocytes (cyan) at 2–3 d.p.f. Nascent sheaths are indicated with black arrowheads, and processes are indicated with magenta arrowheads. **f**, Enrichment of PSD-95-GFP and GFP-gephyrin puncta in processes and sheaths of differentiating oligodendrocytes.  $n = 12$  and 14 from at least 10 fish each condition. All data are represented as the mean  $\pm$  s.e.m.; two-sided ratio-paired  $t$ -test (**c** and **d**); two-sided Wilcoxon matched-pairs signed-rank test (**f**); scale bars, 5  $\mu$ m.

especially susceptible to photobleaching during long-term imaging; therefore, we generated PSD-95-GFP and GFP-gephyrin constructs and drove their expression with *sox10*, a pan-oligodendrocyte lineage promoter that also labels a subset of interneurons. At 3 d.p.f. in the spinal cord, we found both markers present in punctate and cytosolic forms in OPCs (Fig. 3a), consistent with patterns observed in neurons<sup>26,27</sup>. PSD-95-GFP and GFP-gephyrin puncta size in OPCs resembled that of neurons (Fig. 3a,b and Extended Data Fig. 3a). GFP was enriched in somas, a known phenomenon observed with GFP tagging and knock-in synaptic labeling<sup>28–35</sup>. It is difficult to resolve puncta with such enrichment; therefore, we excluded somas from our analyses. We conducted a series of analyses including puncta number quantification, correlation between puncta number and GFP-tagged protein levels, synaptic alignment, developmental changes and GFP colocalization with antibody staining (Figs. 1e and 2g and Extended Data Figs. 2a and 3b–i). By every applicable metric, we found that PSD-95-GFP and GFP-gephyrin are similar to endogenous labeling by IHC

and FingR.GFP. Next, we examined if these puncta were regulated upon OPC differentiation. We tracked individual OPCs during their development and quantified the GFP-tagged puncta number. Because OPC differentiation takes several hours for all processes to either retract or transform into nascent myelin sheaths<sup>36,37</sup>, we used the disappearance of the last exploratory process as a reference point. We found a decreasing trend during OPC differentiation: puncta numbers reduced from  $9.8 \pm 2.5$  PSD-95-GFP and  $16.5 \pm 2.8$  GFP-gephyrin to  $3.9 \pm 1.2$  PSD-95-GFP and  $9.1 \pm 2.0$  GFP-gephyrin (Fig. 3c,d). In cases where we observed differentiating oligodendrocytes that possessed both processes and myelin sheaths, PSD-95-GFP and GFP-gephyrin puncta were 4-fold and 3.3-fold more enriched in processes than in sheaths, respectively (Fig. 3e,f), suggesting preferential localization of synaptic puncta to processes rather than nascent myelin sheaths. Altogether, these results show a downregulation of GFP-tagged postsynaptic puncta upon OPC differentiation, consistent with reduced synaptic inputs reported from ex vivo electrophysiological studies in rodents<sup>38,39</sup>.

### OPC postsynaptic assembly is dynamic and occurs at hotspots

We next sought to analyze the dynamics of PSD-95-GFP and GFP-gephyrin in OPCs in vivo. These GFP-tagged puncta in OPCs were dynamically assembled and disassembled during an 11-h imaging session, while those in neurons remained relatively stable (Fig. 4a and Supplementary Video 1). The number of puncta per cell remained similar in neurons, but fluctuated in OPCs over 30 min of observation (Fig. 4b). Individual GFP-tagged puncta in neurons lasted about 234 min (PSD-95-GFP) and 206 min (GFP-gephyrin), while those in OPCs lasted about 12 min (PSD-95-GFP) and 5 min (GFP-gephyrin; Fig. 4c). Although photobleaching occurs in FingR.GFP-expressing cells over long periods, short-term imaging is possible. We were therefore able to examine puncta dynamics with FingR.GFP and found similar puncta duration compared to GFP tagging (Fig. 4c). Next, we examined the spatial distribution of GFP-tagged puncta by tracking them in individual OPCs (Fig. 4d). Over the course of 7 h, GFP-gephyrin puncta covered a large space, with a convex hull volume nearly 50 times the volume of an OPC from a single timepoint (Fig. 4d,e). Yet this convex hull volume was not significantly different from the convex hull volume of the OPC over the imaging window, suggesting that GFP-gephyrin assembly stays tuned with OPC process remodeling (Fig. 4d,e). Puncta assembly and disassembly occurred in process regions that were relatively stable as well as those that were remodeled over the imaging window (Fig. 4f,g), suggesting that GFP-tagged puncta dynamics in OPCs were not simply caused by process remodeling. Altogether, GFP-tagged postsynaptic puncta assemble dynamically and cover a large space over time in tune with OPC process remodeling.

Multiple appearances of puncta in the same area (Fig. 4f,g) raises the question if specific regions are preferred for synaptic assembly. To test this, we plotted PSD-95-GFP and GFP-gephyrin puncta over time and overlaid heat maps of puncta frequencies (Fig. 4h,i). We found approximately ten regions ( $1 \mu\text{m} \times 1 \mu\text{m} \times 4 \mu\text{m}$  volumes) per OPC where multiple puncta appeared frequently (3 s.d. above the average) and refer to these regions as hotspots (Fig. 4j). Hotspots represented only 0.3% of GFP-gephyrin puncta space coverage (Fig. 4e). These results suggest that some postsynaptic puncta in OPCs assemble repeatedly and preferentially in the confined spaces of hotspots.

### GFP-gephyrin hotspots in OPCs predict myelin sheath formation

In the zebrafish spinal cord, a myelinating oligodendrocyte forms an average of ten myelin sheaths<sup>36</sup>, similar to the hotspot number we observed per OPC. We wondered if these hotspots in OPCs were associated with future myelin sheath formation. To test this, we conducted long-term imaging of individual OPCs that differentiated and myelinated axons (Supplementary Video 2) and measured the distances from GFP-gephyrin hotspot centers (centroids of  $1 \mu\text{m} \times 1 \mu\text{m} \times 4 \mu\text{m}$ ) to future myelin sheaths (Fig. 5a–d and Methods). In comparison, we selected 30 representative points outside hotspots (non-hotspot) in an OPC. The hotspots were mostly in proximity to future myelin sheaths

(Fig. 5e), and the hotspot–sheath distance was significantly smaller than the non-hotspot–sheath distance (Fig. 5f). Further, we examined the percentage of hotspots or non-hotspots that predicted where future myelin sheaths formed. We chose  $1 \mu\text{m}$  as a threshold because we analyzed previous electron microscopy datasets<sup>40</sup> and our IHC images and found a distance of  $1.4\text{--}1.6 \mu\text{m}$  between two myelinated axons in the dorsal spinal cord (Extended Data Fig. 4a–c). Within  $1 \mu\text{m}$ ,  $29.6\% \pm 8.7\%$  of hotspots in an OPC predicted future sheath locations, while only  $5.9\% \pm 3.4\%$  of non-hotspots did (Fig. 5g). Consistent with this result,  $31.2\% \pm 7.1\%$  of puncta in the hotspot region predicted future myelin sheaths, significantly higher than the prediction by puncta outside ( $15.1\% \pm 3.4\%$ ) or by chance ( $5.5\% \pm 1.1\%$ , myelin volume/OPC survey volume; Extended Data Fig. 4d,e). In addition,  $14.1\% \pm 2.7\%$  of future myelin sheaths in oligodendrocytes were predicted by hotspots in OPCs (Extended Data Fig. 4f), suggesting that hotspots in OPCs predict a subset of myelin sheath formation.

Next, we asked if the relationship between OPC hotspots and future myelin sheaths was dependent on synaptic release. We blocked synaptic release by injecting tetanus toxin (TeNT) into ventricles between 2 and 3 d.p.f. (Fig. 5c). We verified the TeNT delivery to OPCs in the CNS with dextran injection (Extended Data Fig. 4g and Methods). TeNT administration caused a right shift in hotspot–sheath distance distribution (Fig. 5e). The hotspot–sheath distance was no longer significantly smaller than the non-hotspot–sheath distance (Fig. 5f). More importantly, TeNT administration reduced the hotspots' prediction of myelin sheaths (Fig. 5g), the prediction of myelin sheath by GFP-gephyrin puncta in the hotspot regions (Extended Data Fig. 4e) and the percentage of myelin sheaths predicted by hotspots (Extended Data Fig. 4f). This was not due to changes in OPC convex hull volume, OPC hotspot number or myelin sheath number (Extended Data Fig. 4h–j). Together, these results suggest that GFP-gephyrin hotspots can predict myelin sheath locations in a synaptic release-dependent manner.

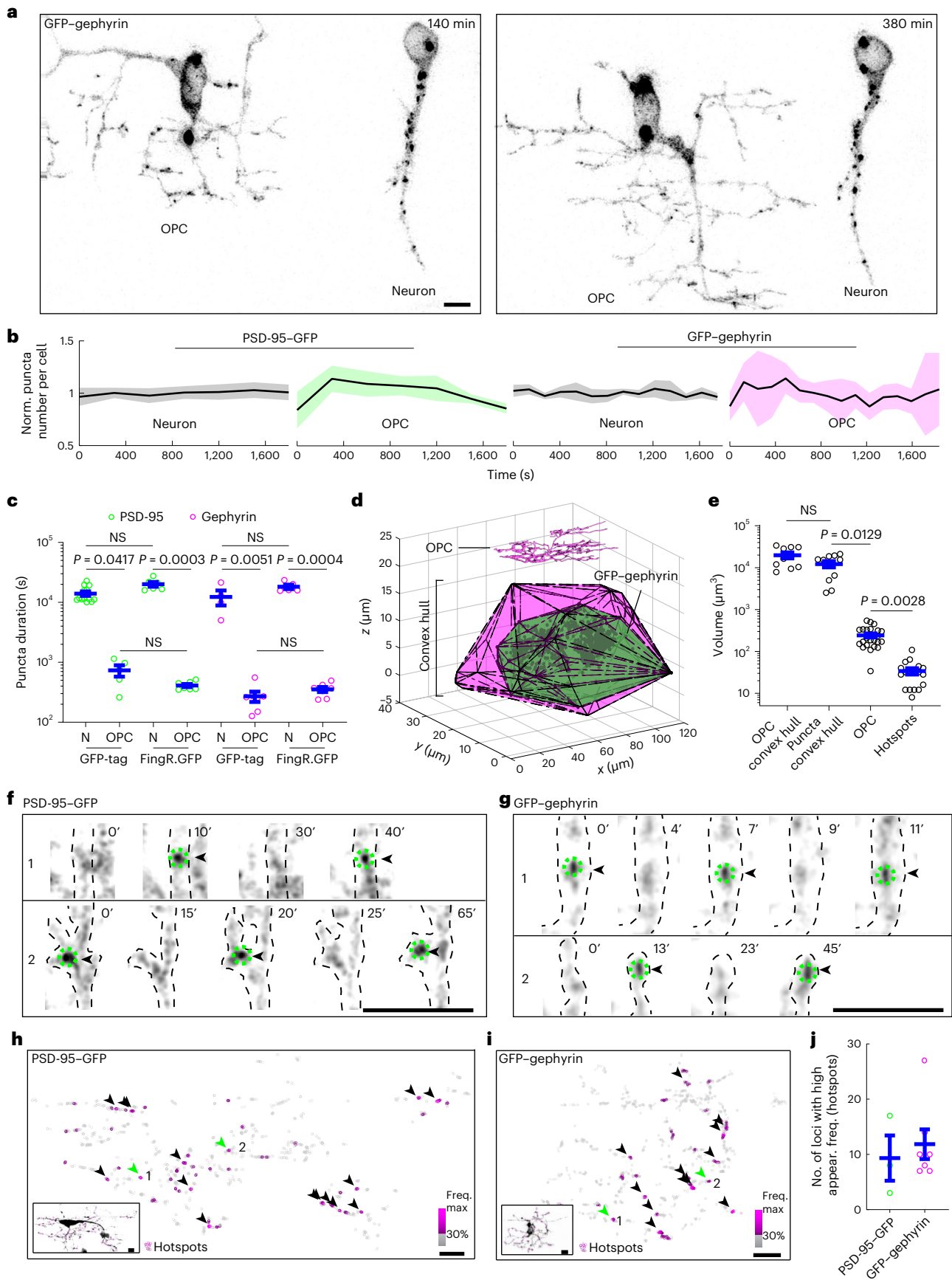
Recent work suggests that early myelination exhibits dynamic and transient ensheathments<sup>37</sup>. We similarly observed this phenomenon (Extended Data Fig. 4k) and wondered if the OPC hotspots could predict transient ensheathments. We found that within  $1 \mu\text{m}$ ,  $32.5\% \pm 7.1\%$  of hotspots in an OPC predicted future transient ensheathment locations in a synaptic release-dependent manner (Extended Data Fig. 4l–n). More importantly, when we combined all ensheathments (stable sheaths and transient ensheathments),  $44.2\% \pm 9.7\%$  of hotspots in an OPC predicted future sheath locations in a synaptic release-dependent manner (Fig. 5h–j). This percentage is higher than prediction by either stable sheaths or transient ensheathments, but lower than the combination of two, suggesting that some hotspots can predict both stable sheaths and transient ensheathments, while others predict only one type.

### MD Ca<sup>2+</sup> activity in OPCs predicts myelin sheath formation

Given the role of Ca<sup>2+</sup> signaling in sheath remodeling<sup>18,41</sup>, we examined the relationship of Ca<sup>2+</sup> signaling events with synapses and sheath

**Fig. 4 | PSD-95-GFP and GFP-gephyrin puncta in OPCs are dynamic and repeatedly assemble at hotspots.** **a**, Representative in vivo images at two timepoints of GFP-gephyrin in a neuron and an OPC next to each other in the spinal cord at 3 d.p.f., related to Supplementary Video 1. **b**, Normalized puncta number per cell of PSD-95-GFP and GFP-gephyrin in neurons and OPCs within 30 min. Black line is the average; shaded area indicates the s.d. From left,  $n = 12$ , 3, 4 and 6 cells from 6, 10, 4 and 4 fish. **c**, Puncta duration in neurons (N) and OPCs at 3 d.p.f. for PSD-95-GFP, FingR.GFP, PSD-95, GFP-gephyrin and FingR.GFP.gephyrin.  $n = 13$ , 5, 6, 7, 4, 7, 5 and 7 cells from at least 4 fish each condition. **d**, Convex hull of OPC processes and GFP-gephyrin puncta over 7 h. The OPC process convex hull is in magenta, and the GFP-gephyrin convex hull is in green. An OPC at a single timepoint is shown on top. **e**, Volumes of OPC process convex hull, GFP-gephyrin puncta convex hull, OPC at a single timepoint and GFP-gephyrin hotspots. From left,  $n = 10$ , 11, 23 and 18 cells from at least 10 fish.

**f,g**, Representative time-lapse images of PSD-95-GFP (**f**) and GFP-gephyrin (**g**) within OPC processes. 1, a relatively stable process; 2, a dynamic process over the imaging time course. The dashed lines outline the process, and arrowheads indicate puncta appearance. Time unit is in minutes. **h,i**, Heat maps of puncta appearance frequency over time for PSD-95-GFP (**h**) and GFP-gephyrin (**i**). 30% of maximum frequency is used as coloring threshold: below threshold, gray; above threshold, a shade of magenta corresponding to the frequency. Loci with high puncta appearance frequency (3 s.d. above average) are marked with arrowheads. The numbers with green arrowheads indicate puncta shown in time-lapse images in **f** and **g**. Bottom left, image of the OPC with puncta marked with magenta circles. **j**, Quantification of loci with high puncta appearance frequency in OPCs. From left,  $n = 3$  and 7 cells from 3 and 5 fish. All data are represented as the mean  $\pm$  s.e.m.; Kruskal–Wallis test followed by uncorrected Dunn's multiple-comparison test (**c** and **e**); scale bars,  $5 \mu\text{m}$ .



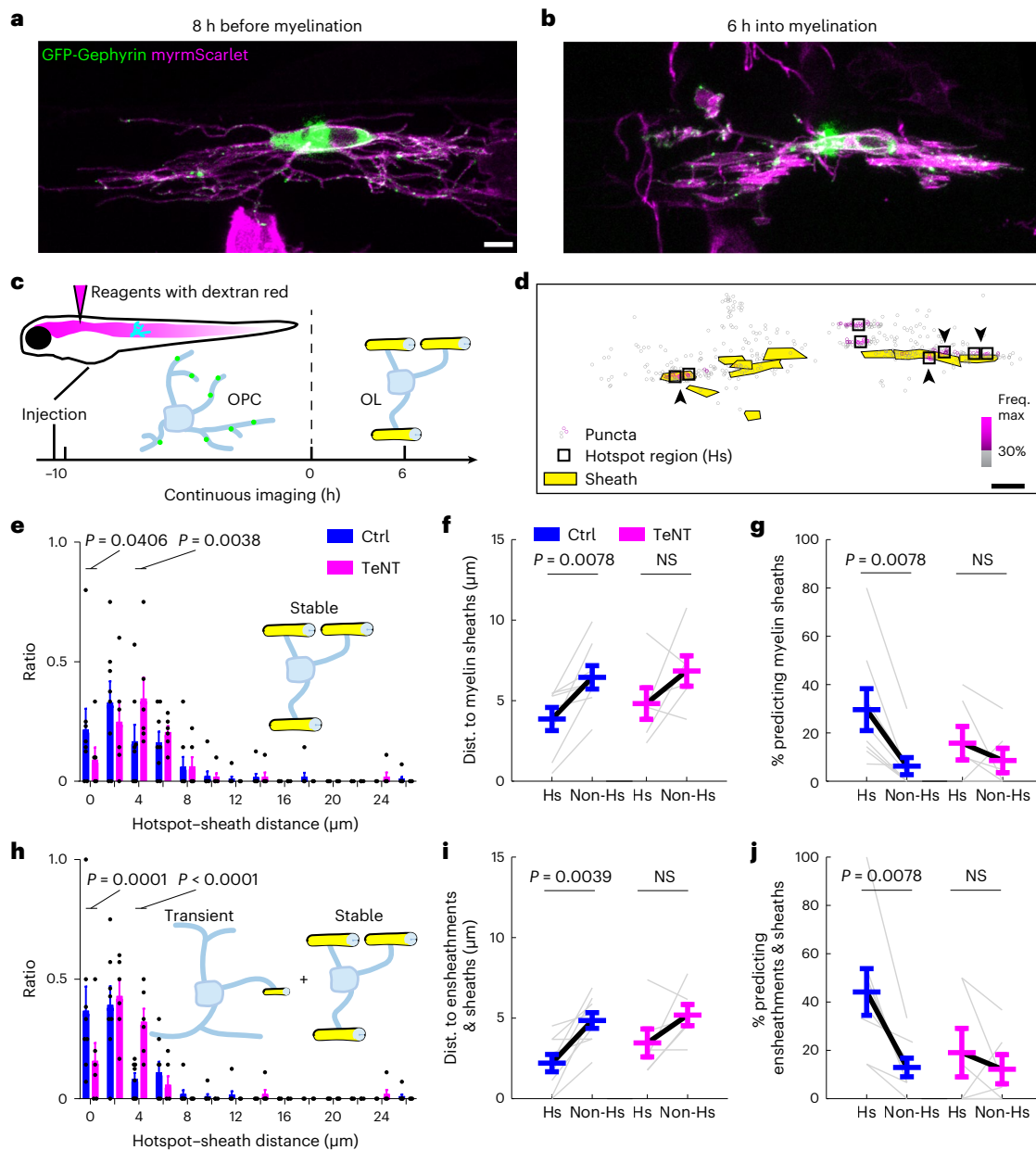


**Fig. 5 | GFP-gephyrin hotspots in OPCs predict a subset of future myelin sheath formation in a synaptic release-mediated manner. a, b,** Representative images of GFP-gephyrin (green) in an oligodendrocyte lineage cell (magenta) at two different stages: OPC stage (a) and oligodendrocyte stage (b), related to Supplementary Video 2. **c,** Schematic showing the imaging protocol of individual OPCs that differentiate into myelinating oligodendrocytes (OLs). The first sheath appearance is designated as time 0. TeNT is delivered through ventricular injection before imaging. **d,** Single-plane merged image of GFP-gephyrin puncta frequency heat map at OPC stage and sheath regions at oligodendrocyte stage. Hotspot regions (black box) and sheaths (yellow) are indicated. Hotspots that exist within where myelin sheaths form are indicated with arrowheads. **e,** Frequency distribution of hotspot-sheath (stable) distances with control and TeNT treatments.  $F[13, 168] = 11.39$ . control,  $n = 8$  cells from 7 fish; TeNT,  $n = 6$  cells from 6 fish. **f,** Quantification of hotspot (Hs)-sheath and non-hotspot

(non-Hs)-sheath (stable) distances with control and TeNT treatments. Control,  $n = 8$  cells from 7 fish; TeNT,  $n = 6$  cells from 6 fish. **g,** Percentage of Hs and non-Hs in an OPC that predict where myelin sheaths (stable) form within 1  $\mu\text{m}$  with control and TeNT treatments. Control,  $n = 8$  cells from 7 fish; TeNT,  $n = 6$  cells from 6 fish. **h,** Frequency distribution of Hs-sheath (all) distances with control and TeNT treatments.  $F[13, 168] = 23.69$ . control,  $n = 8$  cells from 7 fish; TeNT,  $n = 6$  cells from 6 fish. **i,** Quantification of Hs-sheath and non-Hs-sheath (all) distances with control and TeNT treatments. Control,  $n = 8$  cells from 7 fish; TeNT,  $n = 6$  cells from 6 fish. **j,** Percentage of Hs and non-Hs in an OPC that predict where myelin sheaths (all) form within 1  $\mu\text{m}$  with control and TeNT treatments. Control,  $n = 8$  cells from 7 fish; TeNT,  $n = 6$  cells from 6 fish. All data are represented as the mean  $\pm$  s.e.m.; two-sided Wilcoxon matched-pairs signed-rank test (f, g, i and j); two-way analysis of variance (ANOVA) and Fisher's least significant difference test (e and h); scale bars, 5  $\mu\text{m}$ .

formation in vivo. With a plasma membrane-targeted GCaMP6s, we analyzed OPC  $\text{Ca}^{2+}$  activity at single-cell resolution in vivo (Fig. 6a,b). We found that 99% of  $\text{Ca}^{2+}$  events in OPCs occurred in MDs on processes, and 97% of OPCs exhibited only MD  $\text{Ca}^{2+}$  activity during our recordings (Fig. 6c and Supplementary Videos 3 and 4), consistent with recent work in mammals<sup>42,43</sup>. We examined the proximity between  $\text{Ca}^{2+}$

events in MDs and a presynaptic marker, synaptophysin-RFP<sup>17</sup>. Through three-dimensional (3D) reconstruction, we found that  $42\% \pm 6\%$  of MD  $\text{Ca}^{2+}$  events were within a proximity of 0.5  $\mu\text{m}$  to synaptophysin-RFP puncta at 5 d.p.f. (Fig. 6d,e). We also observed that some  $\text{Ca}^{2+}$  events initiated from a 'puncta'-like region in proximity to synapses (Fig. 6f,g). Next, we performed time-lapse imaging to measure the distance from

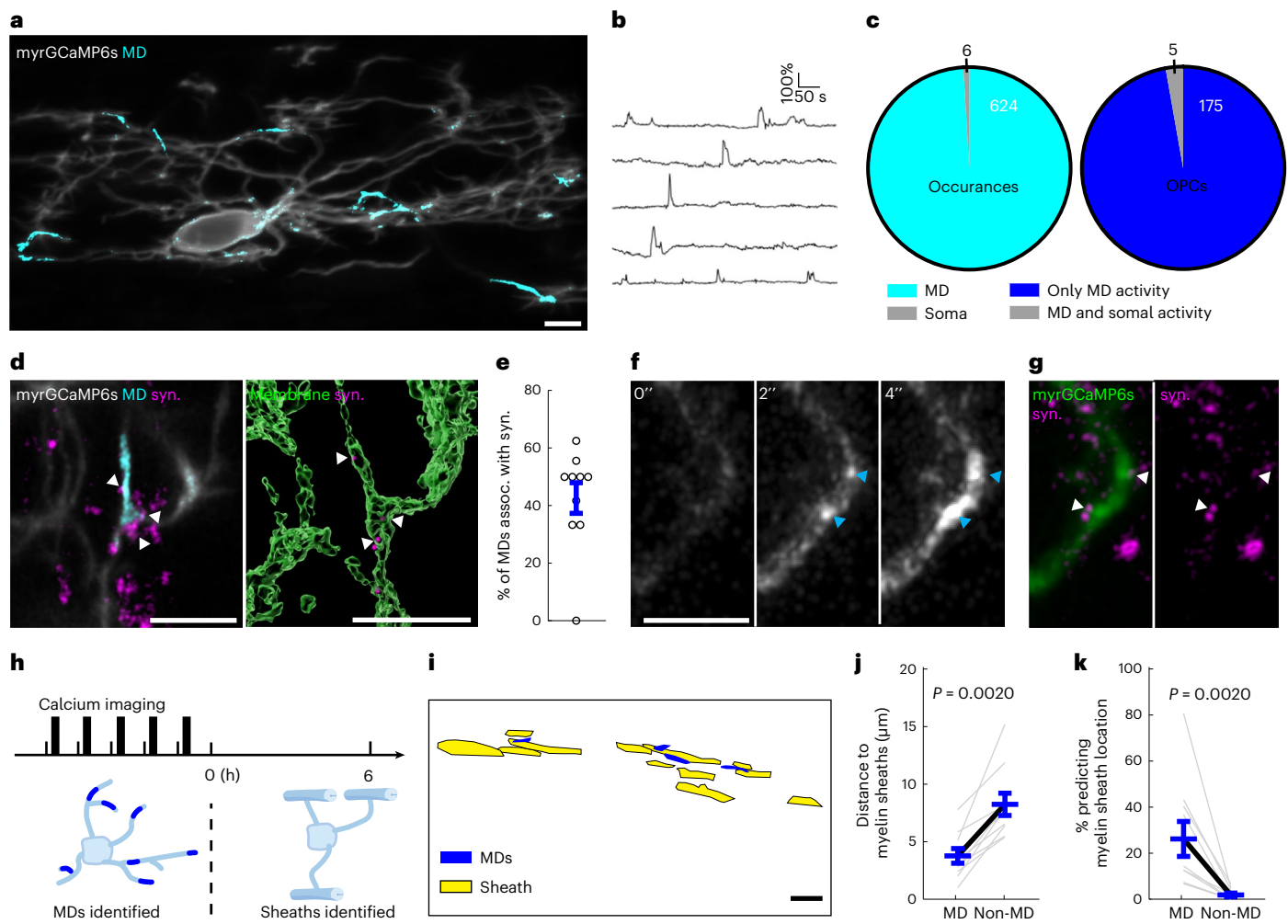


**Fig. 6 | OPC  $\text{Ca}^{2+}$  activity is associated with synapses and predicts myelin sheath formation.** **a**, Representative images of plasma membrane-targeted myrGCaMP6s in an OPC (gray, average projection) showing activity in MDs (cyan). **b**, Individual traces plotting myrGCaMP6s intensity ( $\Delta F/F_{\text{average}}$ ) in five MDs from **a**. Scale bar, 100% and 50 s. **c**, Left, the occurrences of  $\text{Ca}^{2+}$  activity in MDs versus soma; right, the number of OPCs with only MD activity versus OPCs with both MD and somal activity.  $n = 180$  cells from 107 fish. **d**, Left, representative image of a  $\text{Ca}^{2+}$  MD (cyan) in an OPC and presynaptic synaptophysin-RFP (magenta); right, 3D-reconstructed image showing synaptophysin-RFP puncta (magenta) that are within  $0.5 \mu\text{m}$  from MDs (arrowheads). **e**, The percentage of  $\text{Ca}^{2+}$  MDs that are associated with synaptophysin-RFP.  $n = 7$  cells from 7 fish. **f**, Time-lapse images of two  $\text{Ca}^{2+}$  spikes that initiate as puncta and spread to form MDs, indicated by blue arrowheads. The time is in seconds. **g**, The two MDs from **f** initiate in proximity (within  $0.5 \mu\text{m}$ ) to presynaptic synaptophysin-RFP (magenta), indicated by white arrowheads. **h**,  $\text{Ca}^{2+}$  imaging protocol of individual OPCs that differentiate into oligodendrocytes. The first sheath appearance is designated as time 0. Images up to 6 h before time 0 are used to identify OPC  $\text{Ca}^{2+}$  events in MDs, and images around 6 h after time 0 are used to define sheath regions. **i**, Single-plane merged image of  $\text{Ca}^{2+}$  MDs at OPC stage and sheath regions at oligodendrocyte stage.  $\text{Ca}^{2+}$  MDs (blue) and sheaths (yellow) are indicated. **j**, Quantification of MD-sheath and non-MD-sheath distances.  $n = 10$  cells from 8 fish. **k**, Percentage of MDs or non-MDs in an OPC that predict where myelin sheaths form within  $1 \mu\text{m}$ .  $n = 10$  cells from 8 fish. All data are represented as the mean  $\pm$  s.e.m.; two-sided Wilcoxon matched-pairs signed-rank test (**j** and **k**); scale bars,  $5 \mu\text{m}$ .

MD  $\text{Ca}^{2+}$  events in an OPC to sheaths formed after the OPC differentiated and myelinated axons (Fig. 6h,i). In comparison, we selected 30 representative points outside MDs (non-MD) in an OPC (Methods). The MD-sheath distance was significantly smaller than the non-MD-sheath distance (Fig. 6j). Next, we examined the percentage of MDs that predicted where myelin sheaths formed. Within  $1 \mu\text{m}$ ,  $32.0\% \pm 9.4\%$  of MDs in an OPC predicted future sheath locations, while only  $4.3\% \pm 1.2\%$  of non-MDs did (Fig. 6k). These measurements of MD-future sheath are similar to those of hotspots-future sheath, suggesting that MD  $\text{Ca}^{2+}$  activity in OPCs in vivo, along with gephyrin hotspots, predetermines where a subset of myelin sheaths forms.

### Synaptic release contributes to generating OPC $\text{Ca}^{2+}$ activity

Given the close relationship between  $\text{Ca}^{2+}$  activity and synapses, we investigated the role of synapses in OPC  $\text{Ca}^{2+}$  activity in vivo. We

blocked synaptic release by sparsely expressing tetanus toxin light chain (TeNTlc)-tdtomato<sup>44</sup> in axons at 5 d.p.f. (Fig. 7a). Compared to OPCs that neighbored few TeNTlc-expressing axons ( $<4$ , few), those that neighbored many TeNTlc-expressing axons ( $>4$ , many) exhibited significantly reduced frequency of  $\text{Ca}^{2+}$  activity ( $0.013 \pm 0.002$  versus  $0.020 \pm 0.002$  Hz), peak amplitude ( $1.4 \pm 0.08$  versus  $1.81 \pm 0.12$  fold), basal signal intensity ( $0.74 \pm 0.06$  versus  $1.00 \pm 0.10$ ) and MD length ( $6.00 \pm 0.25$  versus  $7.03 \pm 0.38 \mu\text{m}$ ; Fig. 7b,c and Extended Data Fig. 5a). Next, we delivered TeNT proteins to the CNS through ventricle injection at 5 d.p.f. and analyzed  $\text{Ca}^{2+}$  activity before and after injection (Fig. 7d). We co-injected dextran (MW 3,000) and verified that dextran surrounded OPCs before  $\text{Ca}^{2+}$  imaging (Fig. 7e). While control solution administration had no effect, TeNT administration led to nearly a 45% reduction in MD event number and frequency of  $\text{Ca}^{2+}$  activity (Fig. 7f,g, Extended Data Fig. 5b and Supplementary Video 5). These results

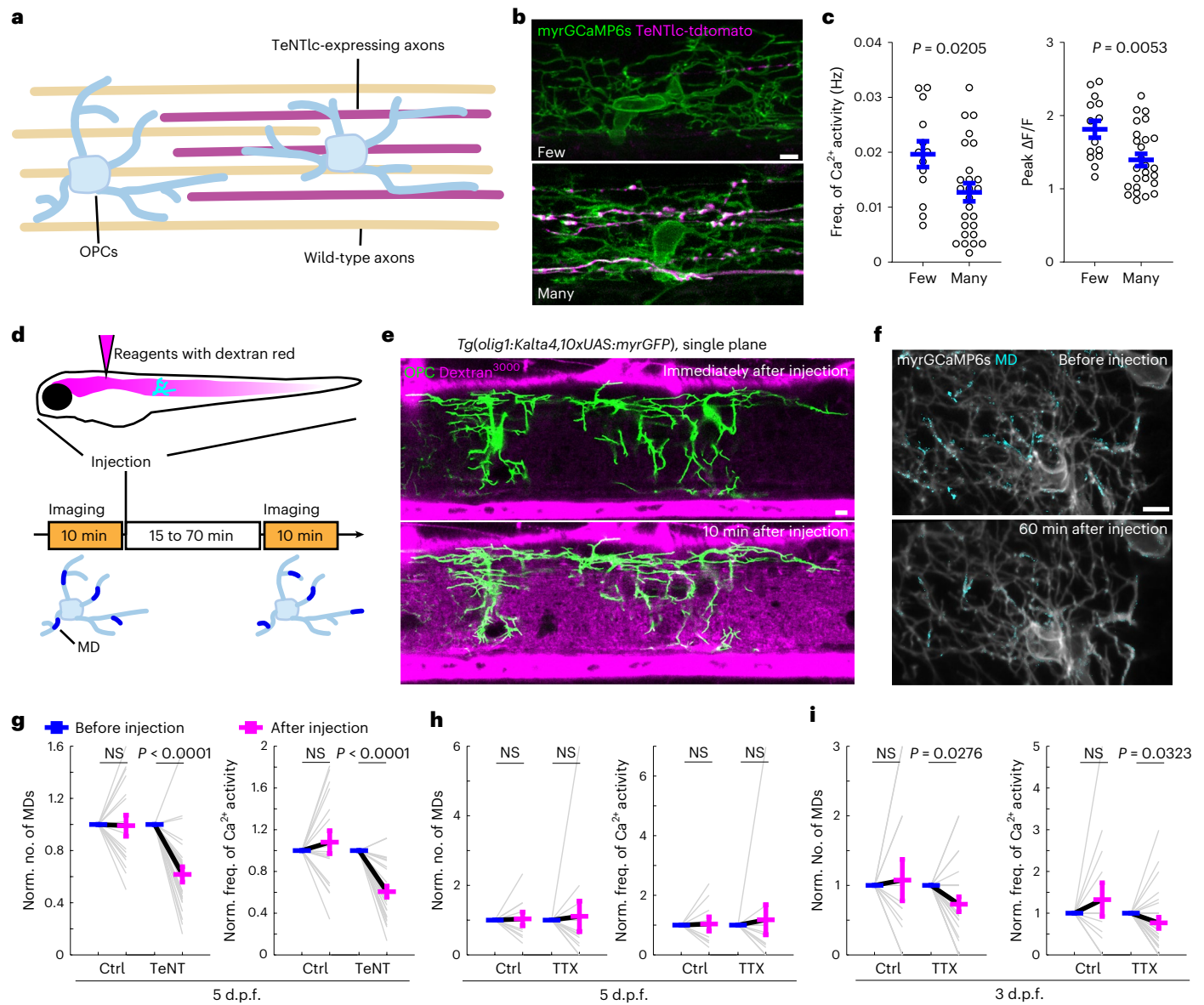


**Fig. 7 | Synaptic release contributes to generating OPC Ca<sup>2+</sup> activity in vivo.** **a**, Schematic showing OPCs neighboring few and many TeNTlc-expressing axons with the sparse-labeling approach. **b**, Representative images of OPCs neighboring few (<4) and many (≥ 4) axons expressing TeNTlc-tdtomato. **c**, The frequency of Ca<sup>2+</sup> activity and peak amplitude in OPCs that neighbor few (<4) and many (≥4) TeNTlc-expressing axons at 5 d.p.f. Few, *n* = 14 cells from 8 fish; many, *n* = 26 cells from 15 fish; *t*[37] = 2.420 and *t*[38] = 2.958. **d**, Experimental paradigm of reagent delivery and Ca<sup>2+</sup> imaging. **e**, Representative single-plane images of individual spinal cord OPCs immediately and 10 min after ventricle injection of dextran<sup>3000</sup> Texas Red (magenta) in *Tg(olig1:Kalta4,10xUAS:myrGFP)* animals. **f**, Representative images of myrGCaMP6s (gray, average projection) and Ca<sup>2+</sup> MDs (cyan) with control and TeNT treatment. **g**, Normalized Ca<sup>2+</sup> MD number and

frequency of Ca<sup>2+</sup> activity in OPCs before (blue) and after (magenta) injection of control or TeNT solution at 5 d.p.f. Paired data are indicated with gray lines. Control, *n* = 17 from 13 fish; TeNT, *n* = 26 cells from 18 fish. **h**, Normalized Ca<sup>2+</sup> MD number and frequency of Ca<sup>2+</sup> activity in OPCs before (blue) and after (magenta) injection of control or TTX solution at 5 d.p.f. Paired data are indicated with gray lines. From left, *n* = 10 and 13 cells from 6 and 9 fish. **i**, Normalized Ca<sup>2+</sup> MD number and frequency of Ca<sup>2+</sup> activity in OPCs before (blue) and after (magenta) injection of control or TTX solution at 3 d.p.f. Paired data are indicated with gray lines. From left, *n* = 13 and 29 cells from 7 and 13 fish. All data are represented as the mean ± s.e.m.; two-sided unpaired *t*-test (**c**) or two-sided Wilcoxon matched-pairs signed-rank test (**g–i**); scale bars, 5 μm.

suggest an important role for synaptic release in OPC Ca<sup>2+</sup> activity. TeNT administration also increased peak duration and MD area, suggesting that the synapse-dependent Ca<sup>2+</sup> activity is associated with shorter duration and smaller MDs.

These effects could be due to reduced neuronal activity and evoked synaptic release by TeNT. But to our surprise, we found that blocking neuronal action potentials with the voltage-gated Na<sup>+</sup> channel blocker tetrodotoxin (TTX) had no effect on the OPC Ca<sup>2+</sup> activity at 5 d.p.f. (Fig. 7h and Extended Data Fig. 5c). We excluded the possibility of ineffective TTX delivery in three ways: we observed larval paralysis

within 3 min after injection (30/30), a complete block of motor neuron Ca<sup>2+</sup> activity (Extended Data Fig. 5d,e) and dextran co-injected with TTX (dextran MW 3,000, larger than TTX) surrounded the imaged OPCs (120/120). Therefore, the reduced Ca<sup>2+</sup> activity upon TeNT injection was most likely because of TeNT on spontaneous release at neuron–OPC synapses, rather than neuronal activity. We did, however, observe reduced OPC Ca<sup>2+</sup> activity upon TTX injection at the earlier timepoint of 3 d.p.f. (Fig. 7i and Extended Data Fig. 5f), consistent with a previous report<sup>18</sup> and suggesting a diminishing role of neuronal activity and evoked synaptic release over development. Altogether,

our results establish a role for synaptic release in generating OPC  $\text{Ca}^{2+}$  activity in vivo.

### Synaptic disruption impairs OPC development and myelination

Previous studies found that blocking neuronal activity and presynaptic release could impair myelination<sup>10,12</sup>. Given how GFP–gephyrin assembly and  $\text{Ca}^{2+}$  activity in OPCs predict myelin sheath formation in a synaptic release-dependent manner, we next sought to examine the role of postsynaptic molecules in OPC development and myelination. We reasoned that disruption of these molecules could impair OPC development and myelination, because without them, OPCs would have to bypass the lack of presynaptic inputs to differentiate and choose axons for myelination. We developed and verified a cell-specific CRISPR–Cas9-mediated gene disruption system (Extended Data Fig. 6). Besides *dlg4a/dlg4b* and *gphnb* (Methods), which are important for excitatory and inhibitory synapses, respectively, we also targeted *nlg3*, because it is highly expressed in OPCs (Extended Data Fig. 1a,b)<sup>17,19</sup>, localized to neuron–OPC synapses (Extended Data Fig. 7a–d), important for MAGUK and gephyrin density (Extended Data Fig. 7e,f) and  $\text{Ca}^{2+}$  activity in OPCs (Extended Data Fig. 7g–i). To examine if OPC differentiation is affected by disruption of these postsynaptic molecules, we calculated the ratio of myelinating oligodendrocytes at different stages of development and found that *nlg3b* disruption in oligodendrocyte lineage cells led to fewer myelinating oligodendrocytes and more OPCs (Fig. 8a–c). To assess myelination, we measured the number and total length of nascent myelin sheaths. *dlg4a/dlg4b* or *gphnb* disruption reduced the total length of myelin sheaths at 5 d.p.f. (Fig. 8d–f). *nlg3b* disruption resulted in a reduction in the number and total length of myelin sheaths at both 3 d.p.f. and 5 d.p.f. (Fig. 8d–f and Extended Data Fig. 8a,b). Overexpression of a presumed dominant-negative Nlg3b ( $\Delta 116$ ) that lacks C-terminal domains required for interaction with MAGUK and gephyrin<sup>23,45</sup> (Extended Data Fig. 8c) also led to a reduction in the total length of myelin sheaths (Fig. 8f). In addition, among myelinating oligodendrocytes, we noted that  $7.6\% \pm 1.8\%$  upon *nlg3b* disruption possessed cytoplasmic processes with abnormal trapezoidal structures (Fig. 8g and Extended Data Fig. 8d,e), suggestive of defective OPC differentiation. Together, these results support a role for postsynaptic molecules in proper OPC differentiation and myelination.

### Discussion

The landmark discovery of neuron–OPC synapses over 20 years ago has inspired a number of studies to examine their properties with electrophysiology and electron microscopy<sup>4</sup>, yet we still lack basic understanding of their assembly and function. Here, we establish an in vivo model of these synapses in zebrafish OPCs (Fig. 8h): they are composed of postsynaptic MAGUK (PSD-95) and gephyrin and are developmentally regulated; they exhibit a wide range of alignment with synaptic partners and dynamic synapse features; they cover large spatial volumes over time but frequently and repeatedly assemble

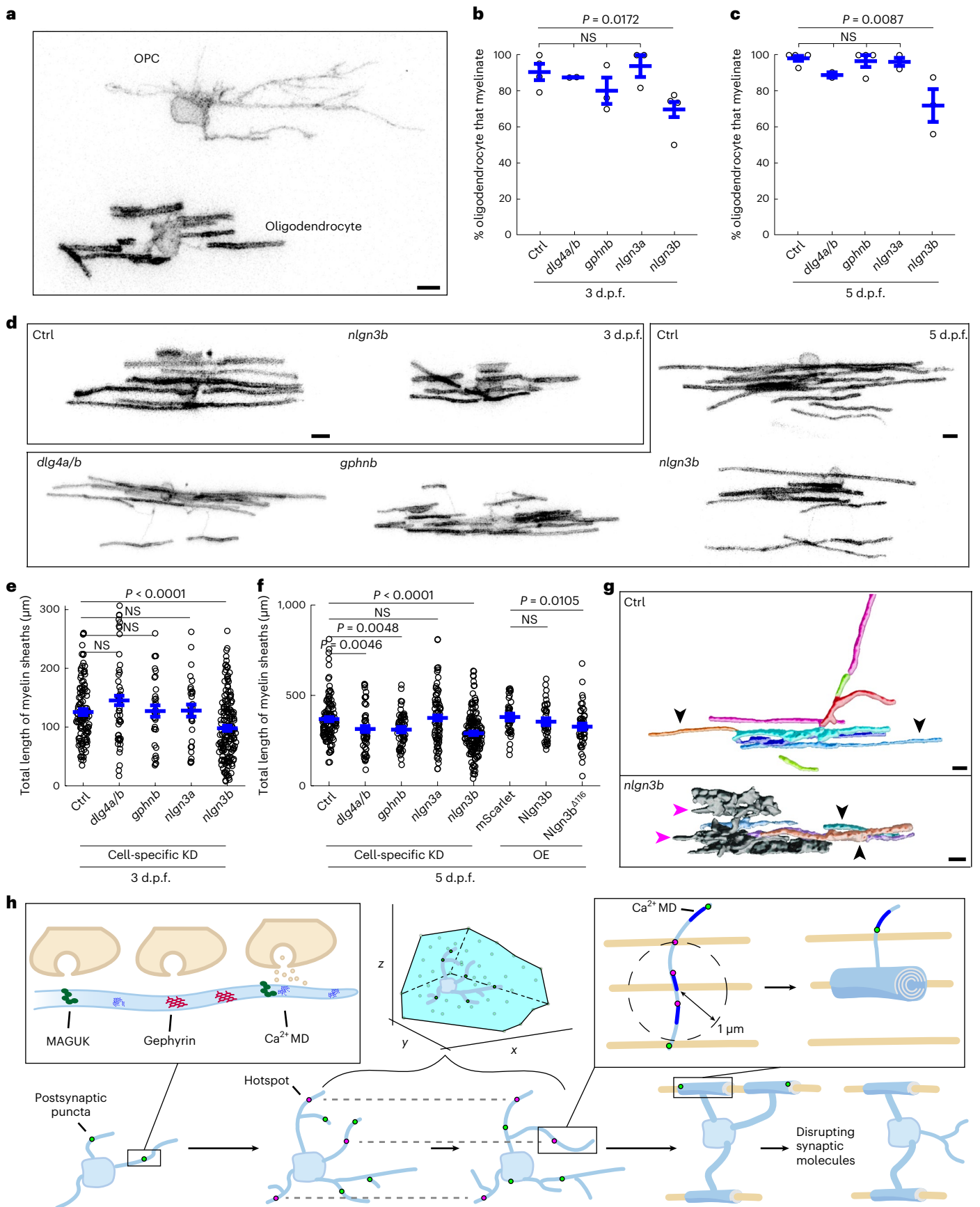
at specific and confined ‘hotspots’; gephyrin hotspots and synaptic release-mediated  $\text{Ca}^{2+}$  activity partially predict myelination patterns; and disruption of the synaptic molecules PSD-95, gephyrin and Nlg3 impairs OPC development and myelination.

Previous studies suggest that neuronal activity and presynaptic release bias oligodendrocyte myelination to ‘active’ axons<sup>10,12</sup>. However, it is not clear what mechanisms mediate this preference. Here, we identify a postsynaptic mechanism in OPCs that depends on presynaptic release and predicts future myelination, which might partially explain how neuronal activity regulates myelination. We observed an approximately 30% prediction rate with a 1- $\mu\text{m}$  threshold by both GFP–gephyrin hotspots and MD  $\text{Ca}^{2+}$  in OPCs, suggesting they may act in the same pathway to determine where myelin sheaths form. One possible scenario is that presynaptic release from neurons leads to synaptic activation in a nearby OPC process and subsequent  $\text{Ca}^{2+}$  activity in MDs. After the OPC ‘senses’ this neuronal location, it could enhance the synaptic assembly in this location through  $\text{Ca}^{2+}$  signaling. Through such a positive-feedback mechanism, ‘hotspots’ form, while the presynaptic and postsynaptic interactions influence the cytoskeleton to transform a process into a myelin sheath. 14% of stable myelin sheaths were predicted by GFP–gephyrin hotspots, suggesting specificity in prediction and other factors or mechanisms involved, such as PSD-95 hotspots, neurotransmitters or cell adhesion molecules. During OPC differentiation, we and others observed transient ensheathments that disappear rapidly after formation<sup>46</sup>. The GFP–gephyrin hotspots predict the formation of transient ensheathments as well as the stable sheaths, suggesting that similar postsynaptic mechanisms in OPCs guide both transient ensheathment and stable myelin sheath formation. What type of presynaptic release is involved in predetermining myelination patterns? Multiple neurotransmitters and neuropeptides can regulate the development of oligodendrocyte lineage cells<sup>5–8,46</sup>. Therefore, different types of neurons across CNS regions may use a combination of neurotransmitters and/or neuropeptides to influence myelination of their axons. Here, we focus on gephyrin-containing synapses and predict that inhibitory neurotransmitters, such as glycine and GABA, may be involved in regulating the dynamic assembly of gephyrin and OPC development. Meanwhile, how the presynaptic release sites apposed to OPC postsynaptic sites are distributed in neurons is still not fully understood. A recent study suggests presynaptic release sites are assembled in hotspots toward which myelin sheaths grow<sup>47</sup>. Together with our data, this suggests that both presynaptic and postsynaptic sites of neuron–OPC synapses are dynamically assembled at ‘hotspots’ that predetermine where future myelin sheaths form on axons. The presynaptic and postsynaptic alignment at OPC synapses averages 40–50%, suggesting that some synaptic locations miss other synaptic molecules and are likely immature<sup>48–51</sup>. Such alignment ratios and fast synaptic assembly are in tune with an OPC’s dynamic cell biological properties and could allow these cells to effectively survey their environments.

Several studies have identified synaptic mechanisms underlying  $\text{Ca}^{2+}$  elevation in OPCs under conditions of increased neuronal activity

**Fig. 8 | Disruption of postsynaptic molecules impairs OPC development and myelination.** **a**, Representative images of an OPC and an oligodendrocyte in a *nlg3b*-targeted fish. **b, c**, Percentage of oligodendrocytes that myelinate in ctrl-, *dlg4ab*-, *gphnb*-, *nlg3a*- and *nlg3b*-targeted fish at 3 d.p.f. (**b**) and 5 d.p.f. (**c**). 3 d.p.f.,  $n = 144, 57, 49, 41$  and  $193$  cells from  $78, 30, 27, 26$  and  $97$  fish; 5 d.p.f.,  $n = 155, 58, 79, 84$  and  $198$  cells from  $80, 36, 40, 61$  and  $93$  fish. **d**, Representative morphologies with control- (ctrl-), *dlg4ab*-, *gphnb*- and *nlg3b*-targeted oligodendrocytes for cell-specific knockdown at 3 d.p.f. and 5 d.p.f. **e**, Total length of myelin sheaths per oligodendrocyte at 3 d.p.f. in ctrl-, *dlg4ab*-, *gphnb*-, *nlg3a*- and *nlg3b*-targeted oligodendrocytes.  $n = 121, 50, 34, 30$  and  $170$  cells from  $78, 30, 27, 26$  and  $97$  fish. **f**, Total length of myelin sheaths per oligodendrocyte at 5 d.p.f. in ctrl-, *dlg4ab*-, *gphnb*-, *nlg3a*- and *nlg3b*-targeted oligodendrocytes and mScarlet-, Nlg3- and Nlg3 ( $\Delta 116$ )-expressing oligodendrocytes.  $n = 118, 52, 63, 80, 152, 40, 40$  and  $49$  cells from  $80, 36, 40,$

$61, 93, 31, 36$  and  $39$  fish. **g**, Morphology of oligodendrocytes with ctrl- and *nlg3b*-targeted oligodendrocytes for cell-specific knockdown at 5 d.p.f. Top, 3D-reconstructed single oligodendrocyte with sheath (colored) and non-sheath (gray). Sheath (black arrowheads) and processes (magenta arrowheads) are indicated. **h**, In vivo model of neuron–OPC synapses: they are composed of MAGUK and gephyrin and contribute to OPC  $\text{Ca}^{2+}$  activity through spontaneous release; they exhibit fast dynamics, which enable OPCs to survey large spatial volumes; synaptic assembly hotspots and associated  $\text{Ca}^{2+}$  activity at the OPC stage predict where a subset of myelin sheaths forms at the oligodendrocyte stage; synaptic assembly is regulated through development, while disruption of synaptic molecules impairs OPC development and myelination. All data are represented as the mean  $\pm$  s.e.m.; Kruskal–Wallis test followed by uncorrected Dunn’s multiple-comparison test (**b, c, e** and **f**); scale bar,  $5 \mu\text{m}$ . KD, knockdown; OE, overexpression.



(for example, through axon stimulation) with a focus on somal activity<sup>14–16,52</sup>. Interestingly, recent studies provided evidence that neuronal activity or synaptic release contribute little to OPC MD Ca<sup>2+</sup> activity in adult mouse brains<sup>42,43</sup>. Like these studies, we find that OPC Ca<sup>2+</sup> activity in vivo mainly occurs in MDs; in contrast, we show that MD Ca<sup>2+</sup> activity does require synaptic release in the zebrafish spinal cord, suggesting interesting regional and/or developmental differences that will be important for future study. Neuronal activity and evoked synaptic release play a role in OPC Ca<sup>2+</sup> activity at 3 d.p.f., but to our surprise not at 5 d.p.f. Considering that OPC differentiation initiates at 3 d.p.f., this suggests that OPCs are sensitive to neuronal activity through Ca<sup>2+</sup> signaling at this critical stage of development. This sensitivity may be important for OPC differentiation and myelination in development. This development-specific sensitivity to neuronal activity also cautions the usage of axon stimulation that has been widely used in previous studies of OPC Ca<sup>2+</sup> activity<sup>14–16,52</sup>. In our Ca<sup>2+</sup> assays, we observe ‘outlier’ OPCs that behave differently from the majority of OPCs. For example, some OPCs exhibit no change or even an increase of Ca<sup>2+</sup> activity upon TeNT treatment or TTX treatment, while most OPCs exhibit a reduction. These ‘outlier’ OPCs and activity could be due to Ca<sup>2+</sup> generated from synapse-independent mechanisms, such as adrenergic receptor-mediated Ca<sup>2+</sup> activity as recently suggested in cerebral cortex<sup>42,43</sup>. In line with this, nearly 61% of Ca<sup>2+</sup> MDs do not associate with presynaptic markers, and nearly 55% residual Ca<sup>2+</sup> activity remains after TeNT treatment, supporting synapse-independent Ca<sup>2+</sup>-inducing mechanisms in OPCs as well as synapse-dependent mechanisms.

Our findings that *dlg4a/dlg4b*, *gphnb* or *nlg3b* knockdown in oligodendrocyte lineage cells impairs OPC differentiation and myelination suggest a potential role of synapses in OPCs. This is consistent with our observations that GFP–gephyrin hotspots and Ca<sup>2+</sup> MDs in OPCs predict where myelin sheaths form in oligodendrocytes. The myelination defects were not detected until 5 d.p.f. with *dlg4a/dlg4b* or *gphnb* knockdown, but were detected at both 3 and 5 d.p.f. with *nlg3b* knockdown. We reasoned that this was due to Nlgn3’s broader presence and function at glutamatergic, GABAergic and glycinergic synapses. *dlg4a/dlg4b*, *gphnb* or *nlg3b* knockdown approaches likely have larger impacts on OPC activity and influence more OPCs than did disruption of single synaptic receptors from previous studies. In line with our findings, an in vitro study found that incubating neuron–glia co-cultures with extracellular domains of Nlgn3 inhibits OPC differentiation and axon wrapping<sup>53</sup>. Interestingly, disruption of the *nlg3* homologs, *nlg1* or *nlg2*, in oligodendrocytes has no effect on the total myelin sheath length<sup>23</sup>, suggesting that synaptic disruption at the OPC stage rather than the oligodendrocyte stage affects myelination. Although non-synaptic roles of Nlgn3 have been reported in glia<sup>54</sup>, our results suggest a synaptic role of Nlgn3 on OPC development and myelination: close association between Nlgn3 and synapses by IHC and in vivo imaging; reduced MAGUK and gephyrin puncta in OPCs upon *nlg3b* knockdown; reduced myelination by truncated Nlgn3 that lacks MAGUK and gephyrin interaction domains. Moreover, the similar effects on myelination from disruptions of *dlg4a/dlg4b*, *gphnb* and *nlg3b* strongly indicate a role of synapses in OPC development and myelination.

The signaling pathways downstream of synapse/Ca<sup>2+</sup> MDs in OPCs remain to be elucidated. Local Ca<sup>2+</sup> activity might alter the cytoskeleton via Ca<sup>2+</sup>-dependent kinases<sup>55</sup> or affect lipid raft domains to change local signaling<sup>52</sup>. Notably, focal adhesion kinases (FAKs) can affect cell motility and interactions with other cells and are tightly connected to Ca<sup>2+</sup> activity<sup>56</sup>. FAKs promote glioma growth downstream of Nlgn3 in response to neuronal activity<sup>3,57</sup>, and we find that *nlg3* disruption leads to impaired OPC differentiation, reduced oligodendrocyte myelination and abnormal morphology. Therefore, Nlgn3 and FAKs may act downstream of synapses and Ca<sup>2+</sup> signaling to regulate OPC behavior through cytoskeletal rearrangement. Overall, our in vivo

study establishes a relationship between neuronal activity, synaptic assembly and Ca<sup>2+</sup> activity at neuron–OPC synapses, and reveals their roles in predicting where myelin sheaths form in oligodendrocytes. This model inspires future directions to investigate the presynaptic and postsynaptic mechanisms underlying neuron–OPC interactions that regulate OPC development and shape myelination.

## Online content

Any methods, additional references, Nature Portfolio reporting summaries, source data, extended data, supplementary information, acknowledgements, peer review information; details of author contributions and competing interests; and statements of data and code availability are available at <https://doi.org/10.1038/s41593-023-01553-8>.

## References

- Franklin, R. J. M. & Ffrench-Constant, C. Remyelination in the CNS: from biology to therapy. *Nat. Rev. Neurosci.* **9**, 839–855 (2008).
- Xiao, Y., Petrucco, L., Hoodless, L. J., Portugues, R. & Czopka, T. Oligodendrocyte precursor cells sculpt the visual system by regulating axonal remodeling. *Nat. Neurosci.* **25**, 280–284 (2022).
- Venkatesh, H. S. et al. Targeting neuronal activity-regulated neuroligin-3 dependency in high-grade glioma. *Nature* **549**, 533–537 (2017).
- Bergles, D. E. & Richardson, W. D. Oligodendrocyte development and plasticity. *Cold Spring Harb. Perspect. Biol.* **8**, a020453 (2016).
- Lundgaard, I. et al. Neuregulin and BDNF induce a switch to NMDA receptor-dependent myelination by oligodendrocytes. *PLoS Biol.* **11**, e1001743 (2013).
- de Biase, L. M. et al. NMDA receptor signaling in oligodendrocyte progenitors is not required for oligodendrogenesis and myelination. *J. Neurosci.* **31**, 12650–12662 (2011).
- Zonouzi, M. et al. GABAergic regulation of cerebellar NG2 cell development is altered in perinatal white matter injury. *Nat. Neurosci.* **18**, 674–682 (2015).
- Balia, M., Benamer, N. & Angulo, M. C. A specific GABAergic synapse onto oligodendrocyte precursors does not regulate cortical oligodendrogenesis. *Glia* **65**, 1821–1832 (2017).
- Mitew, S. et al. Pharmacogenetic stimulation of neuronal activity increases myelination in an axon-specific manner. *Nat. Commun.* **9**, 306 (2018).
- Hines, J. H., Ravanelli, A. M., Schwindt, R., Scott, E. K. & Appel, B. Neuronal activity biases axon selection for myelination in vivo. *Nat. Neurosci.* **18**, 683–689 (2015).
- Gibson, E. M. et al. Neuronal activity promotes oligodendrogenesis and adaptive myelination in the mammalian brain. *Science* **344**, 1252304 (2014).
- Mensch, S. et al. Synaptic vesicle release regulates myelin sheath number of individual oligodendrocytes in vivo. *Nat. Neurosci.* **18**, 628–630 (2015).
- Nagy, B., Hovhannisyan, A., Barzan, R., Chen, T. J. & Kukley, M. Different patterns of neuronal activity trigger distinct responses of oligodendrocyte precursor cells in the corpus callosum. *PLoS Biol.* **15**, e2001993 (2017).
- Barron, T. & Kim, J. H. Neuronal input triggers Ca<sup>2+</sup> influx through AMPA receptors and voltage-gated Ca<sup>2+</sup> channels in oligodendrocytes. *Glia* **67**, 1922–1932 (2019).
- Sun, W., Matthews, E. A., Nicolas, V., Schoch, S. & Dietrich, D. Ng2 glial cells integrate synaptic input in global and dendritic calcium signals. *Elife* **5**, e16262 (2016).
- Hamilton, N., Vayro, S., Wigley, R. & Butt, A. M. Axons and astrocytes release ATP and glutamate to evoke calcium signals in NG2-glia. *Glia* **58**, 66–79 (2010).
- Marisca, R. et al. Functionally distinct subgroups of oligodendrocyte precursor cells integrate neural activity and execute myelin formation. *Nat. Neurosci.* **23**, 363–374 (2020).

18. Krasnow, A. M., Ford, M. C., Valdivia, L. E., Wilson, S. W. & Attwell, D. Regulation of developing myelin sheath elongation by oligodendrocyte calcium transients in vivo. *Nat. Neurosci.* **21**, 24–30 (2018).
19. Zhang, Y. et al. An RNA-sequencing transcriptome and splicing database of glia, neurons, and vascular cells of the cerebral cortex. *J. Neurosci.* **34**, 11929–11947 (2014).
20. Gross, G. G. et al. Recombinant probes for visualizing endogenous synaptic proteins in living neurons. *Neuron* **78**, 971–985 (2013).
21. Uezu, A. et al. Identification of an elaborate complex mediating postsynaptic inhibition. *Science*. **353**, 1123–1129 (2016).
22. Dempsey, W. P. et al. Regional synapse gain and loss accompany memory formation in larval zebrafish. *Proc. Natl Acad. Sci. USA* **119**, e2107661119 (2022).
23. Hughes, A. N. & Appel, B. Oligodendrocytes express synaptic proteins that modulate myelin sheath formation. *Nat. Commun.* **10**, 4125 (2019).
24. Marques, S. et al. Oligodendrocyte heterogeneity in the mouse juvenile and adult central nervous system. *Science* **352**, 1326–1329 (2016).
25. Spitzer, S. O. et al. Oligodendrocyte progenitor cells become regionally diverse and heterogeneous with age. *Neuron* **101**, 459–471 (2019).
26. Yoshii, A. & Constantine-Paton, M. BDNF induces transport of PSD-95 to dendrites through PI3K-AKT signaling after NMDA receptor activation. *Nat. Neurosci.* **10**, 702–711 (2007).
27. Meier, J. & Grantyn, R. A gephyrin-related mechanism restraining glycine receptor anchoring at GABAergic synapses. *J. Neurosci.* **24**, 1398–1405 (2004).
28. El-Husseini, A. E. -D., Schnell, E., Chetkovich, D. M., Nicoll, R. A. & Brecht, D. S. PSD-95 involvement in maturation of excitatory synapses. *Science* **290**, 1364–1368 (2000).
29. Prange, O., Wong, T. P., Gerrow, K., Wang, Y. T. & El-Husseini, A. A balance between excitatory and inhibitory synapses is controlled by PSD-95 and neuroligin. *Proc. Natl Acad. Sci. USA* **101**, 13915–13920 (2004).
30. Saiyed, T. et al. Molecular basis of gephyrin clustering at inhibitory synapses: role of G- and E-domain interactions. *J. Biol. Chem.* **282**, 5625–5632 (2007).
31. Dejanovic, B. et al. Palmitoylation of gephyrin controls receptor clustering and plasticity of GABAergic synapses. *PLoS Biol.* **12**, e1001908 (2014).
32. Oh, W. C., Lutz, S., Castillo, P. E. & Kwon, H. B. De novo synaptogenesis induced by GABA in the developing mouse cortex. *Science* **353**, 1037–1040 (2016).
33. Fortin, D. A. et al. Live imaging of endogenous PSD-95 using ENABLED: a conditional strategy to fluorescently label endogenous proteins. *J. Neurosci.* **34**, 16698–16712 (2014).
34. Fang, H., Bygrave, A. M., Roth, R. H., Johnson, R. C. & Hugarir, R. L. An optimized CRISPR/Cas9 approach for precise genome editing in neurons. *Elife* **10**, e65202 (2021).
35. Ifrim, M. F., Janusz-Kaminska, A. & Bassell, G. J. Development of single-molecule ubiquitination mediated fluorescence complementation to visualize protein ubiquitination dynamics in dendrites. *Cell Rep.* **41**, 111658 (2022).
36. Czopka, T., French-Constant, C. & Lyons, D. A. Individual oligodendrocytes have only a few hours in which to generate new myelin sheaths in vivo. *Dev. Cell* **25**, 599–609 (2013).
37. Almeida, A. R. & Macklin, W. B. Early myelination involves the dynamic and repetitive ensheathment of axons which resolves through a low and consistent stabilization rate. *Elife* **12**, e82111 (2023).
38. Kukley, M., Nishiyama, A. & Dietrich, D. The fate of synaptic input to NG2 glial cells: Neurons specifically downregulate transmitter release onto differentiating oligodendroglial cells. *J. Neurosci.* **30**, 8320–8331 (2010).
39. De Biase, L. M., Nishiyama, A. & Bergles, D. E. Excitability and synaptic communication within the oligodendrocyte lineage. *J. Neurosci.* **30**, 3600–3611 (2010).
40. Hildebrand, D. G. C. et al. Whole-brain serial-section electron microscopy in larval zebrafish. *Nature* **545**, 345–349 (2017).
41. Baraban, M., Koudelka, S. & Lyons, D. A. Ca<sup>2+</sup> activity signatures of myelin sheath formation and growth in vivo. *Nat. Neurosci.* **21**, 19–25 (2018).
42. Lu, T. Y. et al. Norepinephrine modulates calcium dynamics in cortical oligodendrocyte precursor cells promoting proliferation during arousal in mice. *Nat. Neurosci.* **26**, 1739–1750 (2023).
43. Fiore, F. et al. Norepinephrine regulates calcium signals and fate of oligodendrocyte precursor cells in the mouse cerebral cortex. *Nat. Commun.* **14**, 8122 (2023).
44. Koudelka, S. et al. Individual neuronal subtypes exhibit diversity in CNS myelination mediated by synaptic vesicle release. *Curr. Biol.* **26**, 1447–1455 (2016).
45. Shipman, S. L. et al. Functional dependence of neuroligin on a new non-PDZ intracellular domain. *Nat. Neurosci.* **14**, 718–726 (2011).
46. Osso, L. A., Rankin, K. A. & Chan, J. R. Experience-dependent myelination following stress is mediated by the neuropeptide dynorphin. *Neuron* **109**, 3619–3632 (2021).
47. Almeida, R. G. et al. Myelination induces axonal hotspots of synaptic vesicle fusion that promote sheath growth. *Curr. Biol.* **31**, 3743–3754 (2021).
48. Gerrow, K. et al. A preformed complex of postsynaptic proteins is involved in excitatory synapse development. *Neuron* **49**, 547–562 (2006).
49. Panzer, J. A. et al. Neuromuscular synaptogenesis in wild-type and mutant zebrafish. *Dev. Biol.* **285**, 340–357 (2005).
50. Wierenga, C. J., Becker, N. & Bonhoeffer, T. GABAergic synapses are formed without the involvement of dendritic protrusions. *Nat. Neurosci.* **11**, 1044–1052 (2008).
51. Villa, K. L. et al. Inhibitory synapses are repeatedly assembled and removed at persistent sites in vivo. *Neuron* **89**, 756–769 (2016).
52. Wake, H., Lee, P. R. & Fields, R. D. Control of local protein synthesis and initial events in myelination by action potentials. *Science* **333**, 1647–1651 (2011).
53. Proctor, D. T. et al. Axo-glial communication through neuroligin-neuroligin signaling regulates myelination and oligodendrocyte differentiation. *Glia* **63**, 2023–2039 (2015).
54. Stogsdill, J. A. et al. Astrocytic neuroligins control astrocyte morphogenesis and synaptogenesis. *Nature* **551**, 192–197 (2017).
55. Waggner, C. T., Dupree, J. L., Elgersma, Y. & Fuss, B. CaMKII $\beta$  regulates oligodendrocyte maturation and CNS myelination. *J. Neurosci.* **33**, 10453–10458 (2013).
56. Mitra, S. K., Hanson, D. A. & Schlaepfer, D. D. Focal adhesion kinase: In command and control of cell motility. *Nat. Rev. Mol. Cell Biol.* <https://doi.org/10.1038/nrm1549> (2005).
57. Venkatesh, H. S. et al. Neuronal activity promotes glioma growth through neuroligin-3 secretion. *Cell* **161**, 803–816 (2015).

**Publisher's note** Springer Nature remains neutral with regard to jurisdictional claims in published maps and institutional affiliations.

Springer Nature or its licensor (e.g. a society or other partner) holds exclusive rights to this article under a publishing agreement with the author(s) or other rightsholder(s); author self-archiving of the accepted manuscript version of this article is solely governed by the terms of such publishing agreement and applicable law.

© The Author(s), under exclusive licence to Springer Nature America, Inc. 2024

## Methods

### Experimental model and subject details

We used the following existing zebrafish lines and strains: *Tg(sox10:Kalta4)*<sup>58</sup>, *Tg(olig1:Kalta4)*<sup>17</sup>, *Tg(huc:synaptophysin-RFP)*<sup>17</sup>, *Tg(olig2:dsRed)*, *Tg(sox10:GFP-caax)*, *nacre* and *AB*. The following lines were newly generated for this study: *Tg(10xUAS:myrGCAMP6s)*, *Tg(olig1:myrGCAMP6s)*, *Tg(10xUAS:myrGFP)*, *Tg(10xUAS:myrmScarlet)* and *Tg(olig1:myrmScarlet)*. All experimental fish were crossed into the *nacre* background for optimal optics without pigmentation. The *Kalta4/UAS* system allowed sparse labeling and single-cell analysis. The genotypes of fish used for each experiment are indicated in figure legends. Animals in the fish facility were maintained at 28 °C with a 14 h–10 h light–dark cycle. Larvae and juveniles were nurtured with rotifer suspension and dry food (Gemma 75 and 150, respectively). Adults were fed with a combination of brine shrimp and dry food (Gemma 300). Male and female fish aged 3 to 12 months old were mated; larval fish of 2 d.p.f. to 5 d.p.f. were used for experiments (sex is not determined at these stages in zebrafish). All zebrafish experiments and procedures were performed in compliance with institutional ethical regulations for animal testing and research at Oregon Health and Science University (OHSU). Experiments were approved by the Institutional Animal Care and Use Committee of OHSU. Animal and cell numbers are indicated in the figure legends.

### Tissue sectioning and IHC

To prepare transverse sections, zebrafish larvae at indicated stages were first anesthetized with tricaine and then fixed in 4% PFA, 0.1% Triton at 4 °C overnight. Heads and tails were removed to enable better penetration of fixative. The fish were then washed in PBS, 0.1% Triton for 5 min and passed in 10%, 20% and 30% sucrose in PBS, followed by OCT embedding and cryosectioning of 20–25- $\mu$ m slices. The sections were brought to room temperature for 45 min and rehydrated in PBS, 0.2% Triton for 1 h. Next, 3% BSA, 5% NGS and 0.2% Triton in PBS was used as blocking buffer. Primary antibodies used were: chicken anti-GFP (Invitrogen, A10262; 1:1,000 dilution), mouse anti-Pan-MAGUK (NeuroMab K28/86; 1:500 dilution), mouse anti-gephyrin (Synaptic Systems, 147011; 1:1,000), rabbit anti-synapsin 1/2 (Synaptic Systems, 106002; 1:1,000 dilution), mouse anti-PSD-95 6G6-1C9 (MAB1596; 1:1,000 dilution), rabbit anti-Glycine receptor (Synaptic Systems, 146008; 1:1,000 dilution), mouse anti-SV2 (DSHB AB\_2315387; 1:1,000 dilution) and rabbit anti-Nlgn3 (Nittobo Medical, Af1010; 1:1,000 dilution). The MAGUK antibody was previously validated in zebrafish<sup>59–61</sup>, and we validated gephyrin and Nlgn3 antibody in zebrafish (Supplementary Fig. 1). Secondary antibodies (1:1,000 dilution) used were: A488 anti-chicken, A594 anti-rabbit, A647 anti-mouse IgG1 and A647 anti-mouse (Thermo Fisher). The stained samples were mounted in prolong Glass (Invitrogen, P36980) for at least a day before imaging.

### Plasmid construction

Plasmids were designed and processed using ApE v2.0.61. In zebrafish, *gphn* is duplicated (*gphna* and *gphnb*), and there are multiple isoforms for both genes. All isoforms are almost identical in protein sequence except for the inclusion or exclusion of C3 and C4 cassettes. We amplified several isoforms from cDNA and decided to follow up two: *gphnb* isoform X6 (XM\_021468341) because it encodes a protein that is 96% identical and 98% similar to the rat P1 isoform (NP\_074056.2)<sup>62</sup> that has been used to track synapses previously; and, *gphna* isoform X11 (XM\_017351650.2) because it contains a C3 cassette previously reported to be present in glial cells<sup>63</sup>.

Total RNA was extracted from 3 d.p.f. zebrafish AB larvae (50 fish) using RNAeasy Plus Kit (Qiagen 74134). cDNA was synthesized using SuperScript IV Reverse Transcriptase (Invitrogen). Two sets of primers (Supplementary Table 1) were used to clone the full length *gphna* and *gphnb* using high-fidelity Q5 DNA polymerase, followed

by A-addition and TA cloning into pCRII-TOPO backbones. Using Gibson Assembly (NEB E5510S), we added EGFP to the 5' end and a linker GGGGSGGGGSGGGGS in between and integrated it into pCS 2.1 backbones with an AVR11 digestion site. The 5' end was chosen based on previous imaging studies<sup>62</sup>. In transient injections, GFP–gephyrina and GFP–gephyrin b exhibited similar expression profiles; therefore, we used GFP–gephyrin b for our studies and refer to the GFP–3xGGGGS–gephyrin b as GFP–gephyrin throughout the paper. Using Gateway BP reaction (Invitrogen, 11786100), we generated pME\_ATG–GFP–gephyrin b. Using AVR11 and KPNI-HF, we cut GFP–gephyrin b (without an ATG) from the pCS 2.1 backbone and inserted it in frame into p3E\_p2A to generate p3E\_p2A–GFP–gephyrin b.

*PSD-95/dlg4b* transcript NM\_214728.1 encodes a protein that is 76% identical and 83% similar to rat *Dlg4* (NP\_062567.1) and was thus chosen for use in our studies. We added GFP to the 3' end because N-terminal palmitoylation of PSD-95 is necessary for its synaptic localization and receptor clustering<sup>64,65</sup>. It was cloned from cDNA with primers (Supplementary Table 1) similar to *gphn* as described above. We refer to PSD-95-3xGGGGS–GFP as PSD-95–GFP. We generated pME\_ATG–PSD-95–GFP and p3E\_p2A–PSD-95–GFP constructs.

*nlg3b* transcript XM\_005165182 encodes a protein that is 72% identical and 81% similar to mouse *Nlgn3* (NP\_766520). We synthesized the coding region from XM\_005165182 using IDT Gene Synthesis. For GFP labeling, we inserted GFP at the 3' end with a linker and generated pME\_Nlgn3–GFP. In addition, we generated pME\_Nlgn3 (full length) and pME\_Nlgn3 ( $\Delta$ 116) that misses both domains for interactions with MAGUK and gephyrin<sup>23,45</sup>.

pCAG\_FingR.GFP–gephyrin-CCR5TC (Addgene, 46296) and pCAG\_FingR.GFP–PSD-95-CCR5TC (Addgene, 46295) were used to amplify the coding region with an additional 5' zinc finger binding sequence to regulate their expression<sup>20</sup>, followed by BP reaction to generate pME\_zincfinger\_FingR.GFP–PSD-95-CCR5TC and pME\_zincfinger\_FingR.GFP–gephyrin-CCR5TC constructs.

pME\_myrgFP, pME\_myrmScarlet and pME\_myrrFP-T were generated using PCR and BP reactions, with Fyn myristoylation and palmitoylation domain. p3E\_mScarletcaax was generated using PCR and BP reactions. pGP-CMV-GCaMP6s<sup>66</sup> (Addgene, 40753) was used as a template and three primers were used in a Q5 PCR (15 cycles at 71 °C and 20 cycles at 72 °C) to amplify GCaMP6s and add a Kozak sequence, myr (Fyn myristoylation and palmitoylation domain), attB1 and attB2 sequences. This PCR product was used to generate pME\_myrgCaMP6s using a BP reaction.

We obtained multiple plasmids from Tol2 kits: pDestTol2pA2, pDONR221, p5E\_10xUAS, p3E\_polyA, p3E\_p2A<sup>67</sup>, p5E\_sox10<sub>7.2kb</sub><sup>58</sup>, pDestTol2pACryGFP (pDestTol2GE) and pDestTol2pACrymCherry (pDestTol2RE). Using Gateway LR reactions (Invitrogen, 11791020), we generated multiple plasmids (Supplementary Table 1). We used Mnx1:Gal4 (ref. 68) to drive myrGCaMP6s expression in motor neurons. We used Huc:Kalta4 (ref. 58), UAS:TeNTlc-tdtomato<sup>44</sup> to drive TeNTlc expression in neurons. All constructs generated in this study were fully sequenced.

### Cell-specific CRISPR–Cas9 plasmid construction and CRISPR–Cas9-mediated gene disruption

We used 5xUAS:hsp70 promoter-Cas9-T2A-GFP, U6:sgRNA1;U6:sgRNA2<sup>69</sup> (Addgene, 74009) as a backbone and performed the following modifications: replacement of the 5xUAS:hsp70 promoter with the 10xUAS:E1b-bactin-Kozak promoter because we found the original promoter expressed in many nonspecific cell types when injected into *Tg(sox10:Kalta4)*; replacement of T2A-GFP with myrmScarlet-p2A and added to the 5' end of Cas9; addition of polyA to the 3' end of Cas9. Four sets of primers and two previously made plasmids (Tol2-10xUAS:E1b-mScarlet and Tol2-10xUAS:cas9-P2A-RFP-caax) were used to generate four segments. These segments were integrated into the backbone by NEBuilder HiFi assembly (NEB, E2621S).

The new construct is referred to as 10xUAS:myrmScarlet-p2A-Cas9, U6:sgRNA1;U6:sgRNA2.

CHOPCHOP and Crisprscan were used to identify single-guide RNA (sgRNA) sequences for each gene of interest (Supplementary Table 1). The cutting efficiencies of these sgRNAs were verified (>95%) via enzyme digestion of the targeted locus PCR product (CRISPR test primers; Extended Data Fig. 6b). Gel electrophoresis images were taken with Bio-Rad Quantity One 4.6.7. F0 larvae with *gphna* and *gphnb* sgRNA injected together with 1 ng Cas9 protein were used to examine the specificity of the gephyrin antibody. *gphnb* disruption was sufficient to eliminate gephyrin protein in the CNS (Supplementary Fig. 1a,b). BsaI and BsmBI were used to insert the sgRNA into 10xUAS:myrmScarlet-p2A-Cas9, U6:sgRNA1;U6:sgRNA2, while the uninserted plasmid was used as controls. The offspring larvae with sparsely labeled oligodendrocytes were examined for morphology and sheath characteristics.

### Sparse labeling and generation of transgenic lines

Fertilized zebrafish eggs at the one-cell stage were microinjected with 1 nl of an injection solution containing 20 ng  $\mu\text{l}^{-1}$  plasmid DNA, 25 ng  $\mu\text{l}^{-1}$  Tol2 transposase mRNA, 0.02% phenol red and 0.2 M KCl. Injected F0 animals were either used for single-cell analysis or raised to adulthood to generate transgenic lines. To generate stable lines, F1 progenies were screened for germline transmission of the fluorescent reporters. F1 animals were further outcrossed and maintained in the *nacre* background to establish stable transgenic lines with single copy insertion.

### Mounting larvae for in vivo imaging

For most live imaging experiments, larvae were anesthetized with 0.16 mg  $\text{ml}^{-1}$  (600  $\mu\text{M}$ ) tricaine in embryo medium. The fish were mounted in 0.8% low-melting-point agarose (Sigma, A9414) on a coverslip for morphology and sheath examination or in 1.5% low-melting-point agarose in a dish for time-lapse imaging (hours). For gephyrin hotspot and myrGCaMP6s imaging, larvae were immobilized with 0.5 mg  $\text{ml}^{-1}$  non-depolarizing acetylcholine receptor antagonist mivacurium chloride (Abcam) and mounted in 1.5% low-melting-point agarose in a dish.

### Confocal microscopy

All imaging was performed on an upright Zeiss LSM 980 confocal with Airyscan 2 in 4Y fast mode. For fixed tissues, a  $\times 63/1.4$ -NA oil objective was used and for live imaging, a  $\times 20/1.0$ -NA water objective was used. All images were taken using Zeiss software. We used the following lasers: 488 nm for EGFP, myrGCaMP6s and Alexa Fluor 488; 561 nm for RFP, mScarlet, tdTomato, and Alexa Fluor 594; 639 nm for Alexa Fluor 647. Fixed tissue was imaged with 0.15- $\mu\text{m}$  z-spacing with 1.6 $\times$  to 2.5 $\times$  zoom. For in vivo analyses, PSD-95-GFP and GFP-gephyrin were imaged with 2- $\mu\text{m}$  z-spacing at an interval of 5 min (for 30 min to 1 h) or 20 min (for longer than 1 h) at a zoom between 3.7 $\times$  and 10 $\times$  depending on OPC cell size. myrGCaMP6s was imaged with 2- $\mu\text{m}$  z-spacing at 0.5 Hz (four planes scanned) for 10 min or 20 min (drug injection experiments) as previously described<sup>17,18</sup>. Images acquired at 0.5 Hz were analyzed along with images acquired at 10 Hz with a single plane. No major differences were found on the  $\text{Ca}^{2+}$  spike characteristics, but 0.5-Hz acquisition allowed inclusion of more stacks and increased the number of events detected. Therefore, 0.5 Hz was used throughout the study. For tracking OPCs that differentiate into myelinating oligodendrocytes,  $\text{Ca}^{2+}$  imaging was performed repeatedly for 5 min at the beginning of each hour.

### Drug delivery through ventricle injection

For myrGCaMP6s experiments involving drug delivery, we injected drugs via ventricle injection as described previously<sup>18</sup>. In TTX treatment, following 10 min of GCaMP6s imaging, a 1-nl mixture containing 0.2 M KCL, 0.5% dextran Texas Red 3000 MW (Thermo) and  $\text{H}_2\text{O}$

(control) or TTX (0.5 mM, kind gift from H. von Gersdorff's laboratory) was pressure injected into the hindbrain ventricle using an ASI MPPI-3. Between 15 and 35 min after injection, dextran was imaged, followed by another 10 min of GCaMP6s imaging. Dextran surrounding the imaged OPCs was used to verify the drug delivery. TTX caused fish paralysis, further verifying efficient delivery of active drugs. After imaging, fish were removed from mounting media. Larvae injected with control solution recovered full swimming activity within 3 min and TTX-injected paralyzed larvae maintained normal heartbeats for at least 3 h. In TeNT treatment, an 8-nl mixture containing 0.2 M KCL, 0.5% dextran Antonia Red 150,000 MW (Sigma) and TeNT (List Labs, 190A; 0.5  $\mu\text{M}$ ) was pressure injected into the hindbrain ventricle. Between 50 and 70 min after injection, dextran was imaged, followed by another 10 min of GCaMP6s imaging. TeNT-injected larvae showed reduced swimming activity.

### Quantification and statistical analysis

**OPC labeling during development.** We used *sox10* and *olig1* to label OPCs. *sox10* drives expression in both OPCs and myelinating oligodendrocytes while *olig1* labels only OPCs. OPCs and myelinating oligodendrocytes could be distinguished by cell morphology, that is, OPCs only possessed processes and myelinating oligodendrocytes possessed sheaths. Animal ages and corresponding OPC activity were 2 d.p.f. (when OPCs are born and migrate), 3 d.p.f. (when many OPCs initiate differentiation) and 5 d.p.f. (when many OPCs complete differentiation).

**Alignment rate and colocalization ratio.** Images of fixed tissue were analyzed in Imaris. The 'surface' function was used to create a cell surface (smooth and surface grain size = 0.0850  $\mu\text{m}$ ; diameter of largest sphere = 5  $\mu\text{m}$ ; threshold of 900–1,200; number of voxels above 100). The 'spot' function was used to generate Spot<sub>postsynaptic puncta</sub> (estimated xy diameter = 0.35  $\mu\text{m}$ ; estimated z diameter = 0.5  $\mu\text{m}$ ; background subtraction; quality above 2,500 to 2,800). Then, the cell surface was used as a mask to generate Spot<sub>postsynaptic puncta in OPCs</sub>, which was further verified by crosschecking its overlap with Spot<sub>postsynaptic puncta</sub>. Spot<sub>postsynaptic puncta in OPCs</sub> was analyzed for puncta number or density. To examine the alignment of MAGUK (gephyrin) and synapsin, we used the 'spot' function to generate Spot<sub>synapsin puncta</sub>. By determining the proximity of Spot<sub>postsynaptic puncta in OPCs</sub> to Spot<sub>synapsin puncta</sub> using MATLAB-enabled 'colocalize spots' function (<0.1  $\mu\text{m}$ ), we could identify postsynaptic puncta in OPCs that aligned with synapsin and calculate the alignment rate.

For colocalization of PSD-95-GFP (or GFP-gephyrin) and MAGUK (or gephyrin) antibody staining, the 'surface' function was used to create a GFP surface (smooth and surface grain size = 0.0850  $\mu\text{m}$ ; diameter of largest sphere = 6.5  $\mu\text{m}$ ; threshold of 10,000–20,000; number of voxels above 100). We used the Imaris 'coloc' function to generate a coloc channel based on the overlapping pixels between GFP and MAGUK (gephyrin) channels and generated a coloc surface (smooth and surface grain size = 0.0850  $\mu\text{m}$ ; diameter of largest sphere = 6.5  $\mu\text{m}$ ; threshold of 3,000–12,000; number of voxels above 100). We calculated the percentage of GFP that colocalized with antibody staining by dividing the coloc surface volume by the GFP surface volume.

### Postsynaptic puncta identification and analysis from in vivo imaging

Live images of PSD-95-GFP and GFP-gephyrin were processed in ImageJ, and synaptic puncta were identified and tracked with Trackmate<sup>70</sup>. In Trackmate, parameters were set as follows: LOG mode, diameter 0.75  $\mu\text{m}$ , quality > 100, contrast > 0.19 and signal noise > 0.35, LAP linking with 0.5- $\mu\text{m}$  distance and two maximum gap frames allowed were applied. The identified puncta at each frame were then manually examined to remove poor-quality tracks. Neighboring puncta may sometimes be incorrectly linked between time-lapse images; therefore, manual examinations were done to fix these link errors. The data output was analyzed in MATLAB with custom scripts to calculate puncta number per cell at each timepoint, puncta duration and diameter.

To generate figures of mean and s.d. as shade, we used a modified script (<https://www.mathworks.com/matlabcentral/fileexchange/29534-stdshade/>). To analyze the puncta number during OPC differentiation, it was designated as time 0 when a myelinating oligodendrocyte's last process disappeared and all processes transformed into sheaths. In MATLAB, this information is used to divide the puncta number into before and after time 0 for each cell. The traces were generated and realigned based on time 0. To analyze the enrichment of puncta in differentiating oligodendrocytes, the puncta number in sheaths and processes were divided by the corresponding areas and normalized.

**Hotspot analysis.** Heat maps of puncta over time were generated using the output data with Heatscatter (<https://www.mathworks.com/matlabcentral/fileexchange/47165-heatscatter-plot-for-variables-x-and-y/>). With a sampling volume of  $1 \times 1 \times 4 \mu\text{m}$ , regions with frequency higher than three standard deviations were identified as hotspots using custom MATLAB scripts, which also measured the distance between the center of hotspots and future sheaths. The same set of puncta was used to generate the convex hull for GFP–gephyrin. In time-lapse imaging that encompassed both OPC and oligodendrocyte stages, we used the first nascent sheath appearance (time 0) to separate OPC stage and oligodendrocyte stage. It takes up to 5 h for an oligodendrocyte to complete differentiation<sup>36</sup>; therefore, we identified where sheaths formed approximately 6 h after time 0. We grouped the GFP–gephyrin puncta into the ones in hotspot regions and outside hotspot regions. To choose 30 representative points outside hotspots in an OPC, we used Trackmate to convert OPC processes to points and clustered the points outside hotspot regions into 30 groups (non-hotspots) using Lloyd's algorithm in MATLAB. The same set of points was used to generate the convex hull for OPC processes.

The distances between an object (hotspots, non-hotspots, puncta inside hotspots and puncta outside hotspots) and myelin sheaths were measured using custom MATLAB scripts. To examine how such a spot predicted myelin sheaths, we analyzed the frequency distribution of hotspot–sheath distances and calculated the percentage of distances that were less than  $1 \mu\text{m}$ . To control for the myelin sheath prediction by GFP–gephyrin puncta, we calculated the percentage of these puncta that were within  $1 \mu\text{m}$  from myelin sheaths. In comparison, we calculated the random chance by dividing the volume occupied by myelin sheaths by the entire volume occupied by OPCs before differentiation. To estimate the myelin sheath volume, the sheath length and width were measured and the volume was calculated as  $\pi \times \text{length} \times (\text{width}/2)^2$ . To estimate the OPC volume over time, we calculated the volume of the shape generated from process-converted points using Delaunay triangulation.

**Ca<sup>2+</sup> events analysis.** myrGCaMP6s images of z-stacks were maximum projected and stabilized using 'Image Stabilizer'. The images were assigned with random names using 'blindr' (<https://github.com/U8NWXD/blindr/>) before analysis and reassigned with the original names after analysis. The regions of interest (ROIs) showing Ca<sup>2+</sup> event activity were identified by GECIquant<sup>71</sup> first and then manually examined frame by frame. The intensity and area of each ROI were exported and processed in MATLAB through custom scripts. Briefly,  $\Delta F/F_{\text{average}}$  ( $\Delta F = F - F_{\text{average}}$ ) was calculated to generate traces and to identify intensity peaks using 'findpeaks' in MATLAB with filtering parameters (three standard deviations above average, prominence larger than 40% of the baseline and peak area larger than 2.5). Rare elevated Ca<sup>2+</sup> signals for extended periods of time (longer than 50 s) were excluded. Peaks were manually verified against the image. Several Ca<sup>2+</sup> characteristics were measured: peak amplitude, peak duration, Ca<sup>2+</sup> MD number, Ca<sup>2+</sup> MD area and frequency of Ca<sup>2+</sup> activity. A region with multiple OPCs was analyzed for TeNTlc and TeNT experiments, while single OPCs were analyzed for the rest of experiments. To examine the proximity of synaptophysin-RFP to Ca<sup>2+</sup> MDs, Ca<sup>2+</sup> MDs were identified as above,

and their locations were first compared to synaptophysin-RFP manually plane by plane and then verified by Imaris. In Imaris, using the 'spot' and 'surface' functions, we generated synaptophysin-RFP puncta and OPC surface, with which we identified the puncta that were close to OPC surfaces using a MATLAB-enabled 'spot-to-surface' function ( $0.5\text{-}\mu\text{m}$  threshold). These puncta were manually checked against Ca<sup>2+</sup> MDs identified through morphological landmarks in Imaris. The distance between Ca<sup>2+</sup> and future sheaths was measured in MATLAB. In TeNTlc experiments, the number of axons expressing TeNTlc-tdTomato was counted in each image. If the number was less than 4, the corresponding image was grouped as 'neighboring few TeNTlc axons'; otherwise, the image was grouped as 'neighboring many TeNTlc axons'. The distances between Ca<sup>2+</sup> MDs and future myelin sheaths were measured using custom MATLAB scripts. To choose 30 representative points outside MDs in an OPC, we used Trackmate to convert OPC processes to points and clustered the points outside MD regions into 30 groups (non-MD) using Lloyd's algorithm in MATLAB. To examine how MDs or non-MDs predicted myelin sheaths, we analyzed the frequency distribution of MD–sheath and non-MD–sheath distances and calculated the percentage of distances that were less than  $1 \mu\text{m}$ . To examine the Ca<sup>2+</sup> activity in cell-specific knockdown-targeted OPCs, we refined MDs to the mScarlet-labeled processes to analyze only the targeted cells.

**Oligodendrocyte and myelin sheath analysis.** To analyze myelin sheath length and number, we used ImageJ ROI manager to trace all sheaths of sparsely labeled oligodendrocytes between segments 1 and 15 in spinal cord. The number of oligodendrocytes analyzed per fish was limited to 3 to ensure even weight among individual fish. Sheath traces and the corresponding images were blinded using File Name Encrypter in ImageJ. The sheath length and number were then analyzed in MATLAB with custom scripts and matched with the original genotype following analysis. To calculate the myelinating oligodendrocyte percentage, in each imaging experiment, the number of oligodendrocytes from one genotype was counted and divided by the total number of cells (both oligodendrocytes and OPCs). In measuring hotspot–sheath distances, we identified the stable myelin sheaths approximately 6 h after time 0 when processes without terminal sheaths disappeared and all sheaths of oligodendrocytes formed. The transient sheaths were identified similarly to a previous study: larger than  $1.5 \mu\text{m}$  in length and 200% wider than the connected processes. To measure the nearest distance between dorsal myelinated axons with electron microscopy and IHC images, the center of these axons was identified and a nearest point search was performed using a customized MATLAB script.

### Statistics and reproducibility

Most data are shown as mean  $\pm$  s.e.m., with individual data points shown as circles. We conducted Shapiro–Wilk's test and Levene's test to verify data normality and homoscedasticity, respectively, before performing a two-sided *t*-test for unpaired groups, a paired or ratio-paired *t*-test for paired groups and a one-way ANOVA test for more than three groups. If the data did not pass normality tests, we used a Mann–Whitney test for unpaired groups, a Wilcoxon matched-pairs signed-rank test for paired groups, a Friedman test for repeated measures of more than three groups and a Kruskal–Wallis test for more than three groups. These analyses were performed either in GraphPad Prism or MATLAB. The significance and statistical analyses used are indicated in the figure legends. Animal and cell numbers used for each experiment, *t*-values and d.f. for *t*-tests and *F* values and d.f. for ANOVA tests are indicated in figure legends. Data collection was randomized regarding individual animals and cells, and animals were randomly allocated to groups with different treatments. Data collection was not performed blindly due to the experimental conditions, but analyses were performed blindly as indicated. No statistical methods were used to predetermine sample sizes, but our sample sizes are similar to those reported in previous publications<sup>12,17</sup>. Sex is not yet determined

in zebrafish at the ages used in our study and so cannot be considered as a biological variable. No animals or data points were excluded from the specified analyses. Representative experiments (in Figs. 1b,c, 4f,g and 6a,f,g and Extended Data Fig. 6b) were independently replicated a minimum of three times.

### Reporting summary

Further information on research design is available in the Nature Portfolio Reporting Summary linked to this article.

### Data availability

All research materials are available upon request. All reagents generated in this paper will be shared by the corresponding authors upon request. All data reported in this paper will be shared by the corresponding authors upon request. Any additional information required to reanalyze the data reported in this paper is available from the corresponding authors upon request. Source data are provided with this paper.

### Code availability

All original code and custom scripts are available from the corresponding authors upon request. An example script is included in Supplementary Code 1.

### References

58. Almeida, R. G. & Lyons, D. A. Intersectional gene expression in zebrafish using the split KalTA4 system. *Zebrafish* **12**, 377–386 (2015).
59. Meyer, M. P., Trimmer, J. S., Gilthorpe, J. D. & Smith, S. J. Characterization of zebrafish PSD-95 gene family members. *J. Neurobiol.* **63**, 91–105 (2005).
60. Easley-Neal, C., Fierro, J., Buchanan, J. A. & Washbourne, P. Late recruitment of synapsin to nascent synapses is regulated by Cdk5. *Cell Rep.* **3**, 1199–1212 (2013).
61. Sheets, L., Trapani, J. G., Mo, W., Obholzer, N. & Nicolson, T. Ribeye is required for presynaptic Cav1.3a channel localization and afferent innervation of sensory hair cells. *Development* **138**, 1309–1319 (2011).
62. Fuhrmann, J. C. et al. Gephyrin interacts with dynein light chains 1 and 2, components of motor protein complexes. *J. Neurosci.* **22**, 5393–5402 (2002).
63. Smolinsky, B., Eichler, S. A., Buchmeier, S., Meier, J. C. & Schwarz, G. Splice-specific functions of gephyrin in molybdenum cofactor biosynthesis. *J. Biol. Chem.* **283**, 17370–17379 (2008).
64. Craven, S. E., El-Husseini, A. E. & Bredt, D. S. Synaptic targeting of the postsynaptic density protein PSD-95 mediated by lipid and protein motifs. *Neuron* **22**, 497–509 (1999).
65. Topinka, J. R. & Bredt, D. S. N-terminal palmitoylation of PSD-95 regulates association with cell membranes and interaction with K<sup>+</sup> channel Kv1.4. *Neuron* **20**, 125–134 (1998).
66. Chen, T. W. et al. Ultrasensitive fluorescent proteins for imaging neuronal activity. *Nature* **499**, 295–300 (2013).
67. Kwan, K. M. et al. The Tol2kit: a multisite gateway-based construction Kit for Tol2 transposon transgenesis constructs. *Dev. Dyn.* **236**, 3088–3099 (2007).
68. Wyart, C. et al. Optogenetic dissection of a behavioural module in the vertebrate spinal cord. *Nature* **461**, 407–410 (2009).
69. Di Donato, V. et al. 2C-Cas9: a versatile tool for clonal analysis of gene function. *Genome Res.* **26**, 681–692 (2016).
70. Tinevez, J. Y. et al. TrackMate: an open and extensible platform for single-particle tracking. *Methods* **115**, 80–90 (2017).
71. Srinivasan, R. et al. Ca<sup>2+</sup> signaling in astrocytes from *Ip3r2*<sup>-/-</sup> mice in brain slices and during startle responses in vivo. *Nat. Neurosci.* **18**, 708–717 (2015).

### Acknowledgements

This work was supported by an NMSS postdoctoral fellowship FG-1907-34613 (to J.L.), a Warren Alpert Distinguished Scholar Award (to J.L.), NIH/NINDS award F31NS130898 (to T.G.M.) and NIH/NINDS grant 1R21NS120650 (to K.R.M.). We thank D. Bergles, A. Mishra, A. Nechiporuk and members of the laboratory of K.R.M. for discussions and critical reading of the manuscript. We are indebted to A. Forbes, T. Perry and G. Halsell-Vore for fish care. We thank R. Almeida, P. Brehm, M. Freeman, H. von Gersdorff, E. Gouaux, D. Lyons, L. Ma and T. Nicolson for reagents and suggestions as well as F. Coelho, S. Kaech Petrie and the OHSU microscopy core staff for feedback and assistance in imaging. We thank L. Vaskalis for graphic design.

### Author contributions

J.L. conceived the project with input from K.R.M. J.L. carried out experiments and data analyses. T.G.M. generated constructs for *nlg3a* and *nlg3b* disruption, GFP-tagged Nlg3b, and truncated Nlg3b. T.C. provided key resources before their publication. J.L. and K.R.M. wrote the manuscript, and all authors edited and approved the manuscript.

### Competing interests

The authors declare no competing interests.

### Additional information

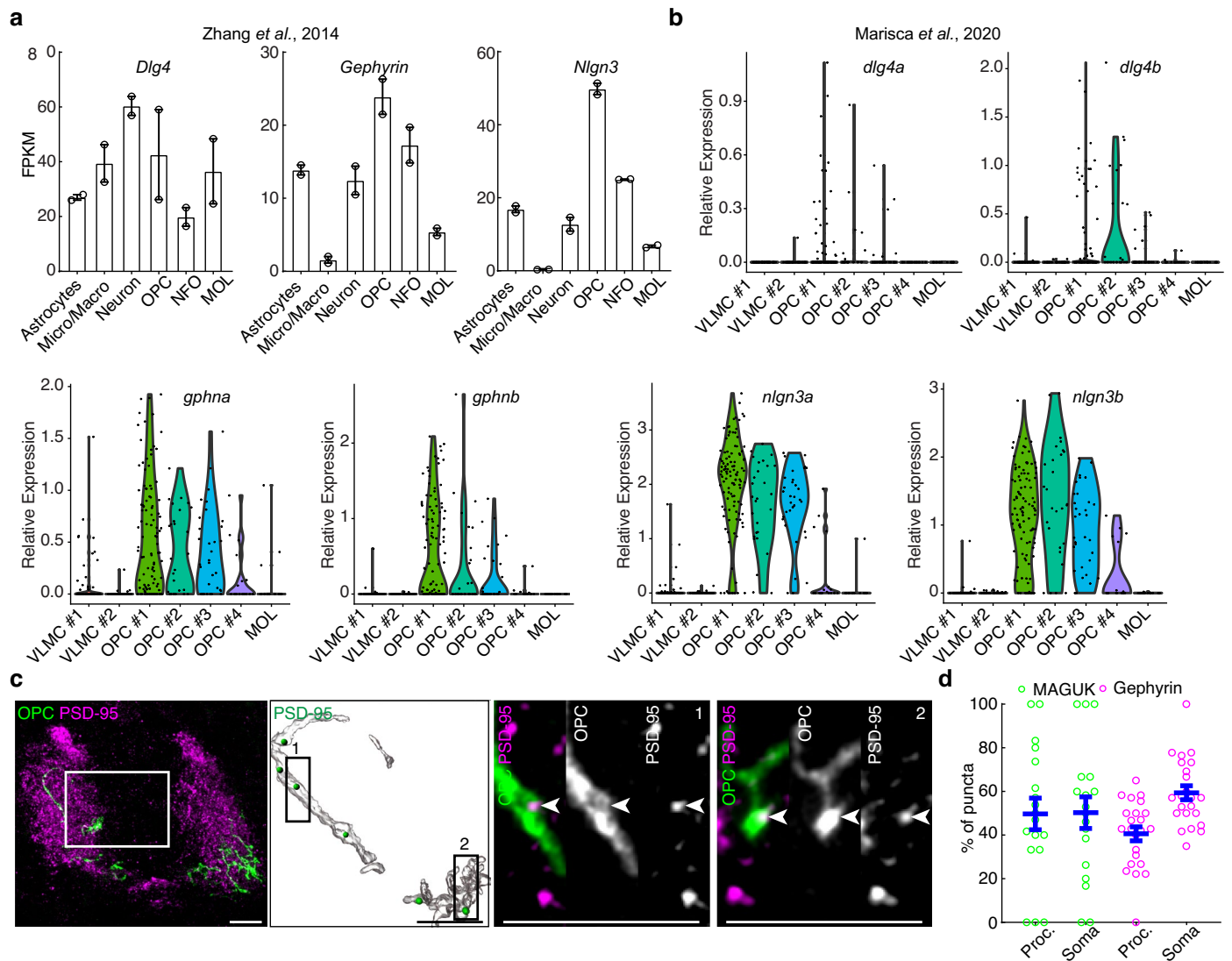
**Extended data** is available for this paper at <https://doi.org/10.1038/s41593-023-01553-8>.

**Supplementary information** The online version contains supplementary material available at <https://doi.org/10.1038/s41593-023-01553-8>.

**Correspondence and requests for materials** should be addressed to Jiaying Li or Kelly R. Monk.

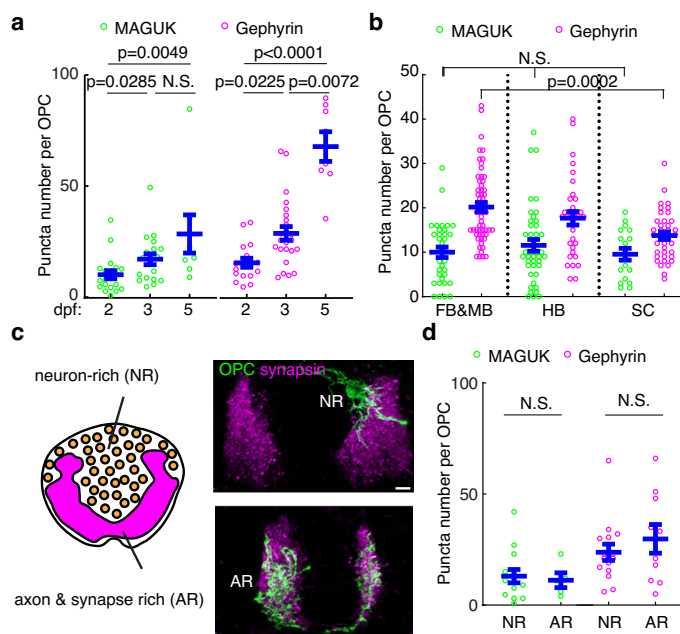
**Peer review information** *Nature Neuroscience* thanks Lucas Cheadle, Robert Hill, and the other, anonymous, reviewer(s) for their contribution to the peer review of this work.

**Reprints and permissions information** is available at [www.nature.com/reprints](http://www.nature.com/reprints).



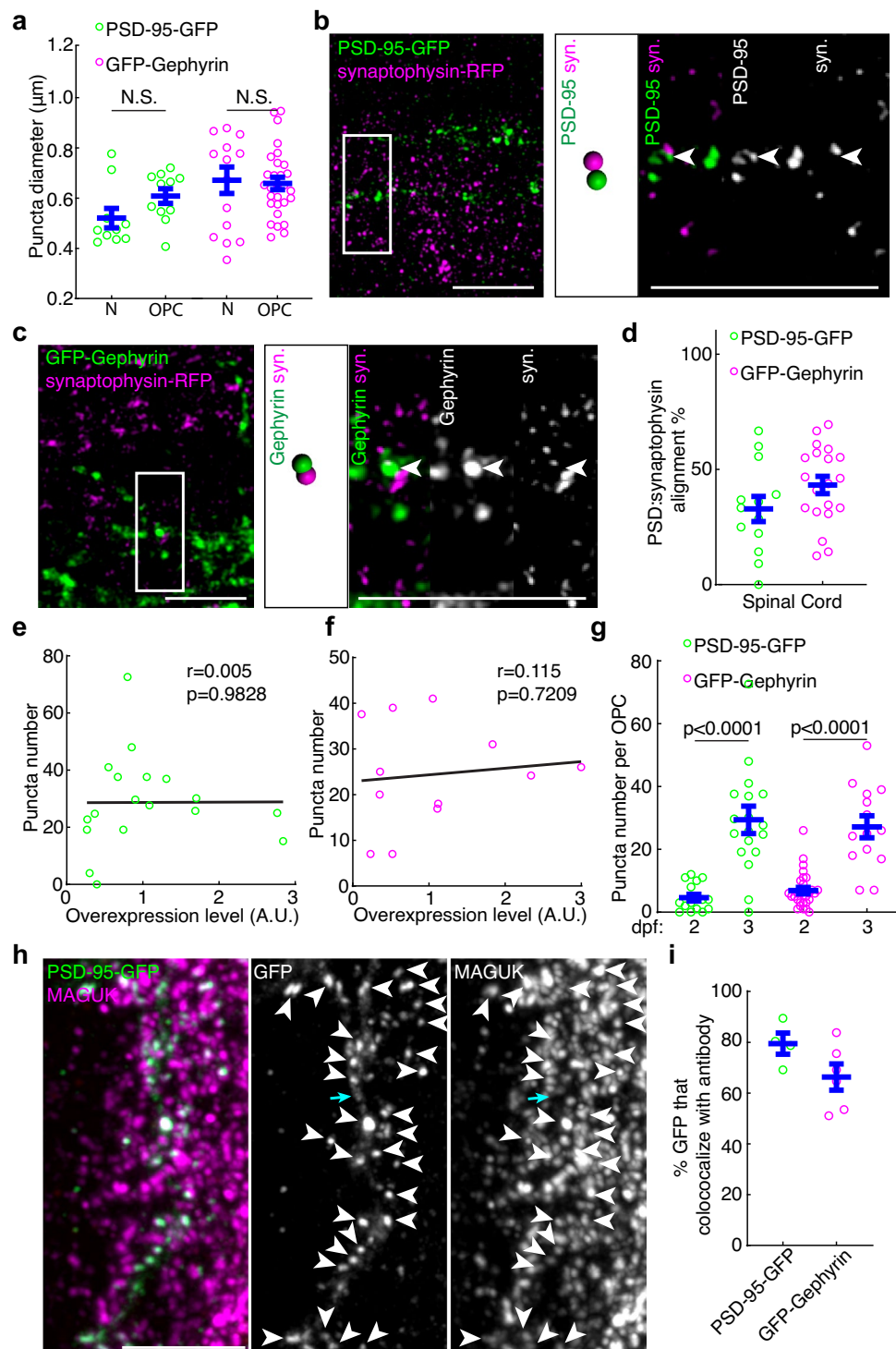
**Extended Data Fig. 1 | MAGUK/PSD-95, Gephyrin, and Nlgn3 are present in OPCs.** (a) RNA-seq expression of murine *Dlg4* (encodes PSD-95), *Gephyrin*, and *Nlgn3* in different CNS cell types<sup>19</sup>. Micro/Macro, Microglia and Macrophage; NFO, Newly-formed oligodendrocyte; MOL, Myelinating oligodendrocyte. n = 2; each biological replicate consists of pooled cells from a litter of 3–12 mice<sup>19</sup>. (b) Single cell RNA-seq expression of zebrafish *dlg4* (a/b), *gephyrin* (a/b), and *nlgn3* (a/b)<sup>17</sup>. VLMC, Vascular leptomeningeal cell; MOL, Myelinating oligodendrocyte. (c) Representative IHC images of PSD-95 in *Tg(olig1:Kal*

*ta4,10xUAS:myrGFP*) spinal cord at 3 d.p.f. From left, spinal cord sections, 3D-reconstructed regions, and two examples of puncta in OPCs at single planes. Only the postsynaptic puncta that fall within OPC process volumes are shown in 3D-reconstructed images (green spheres) and are indicated with arrowheads in examples. In each example, from left are merged channel, OPC channel and PSD-95 channel. (d) % of puncta localized to OPC process (P) and soma (S). MAGUK, n = 18 cells from 8 fish; Gephyrin, n = 40 cells from 15 fish. All data are represented as mean ± SEM; scale bars 5 μm.



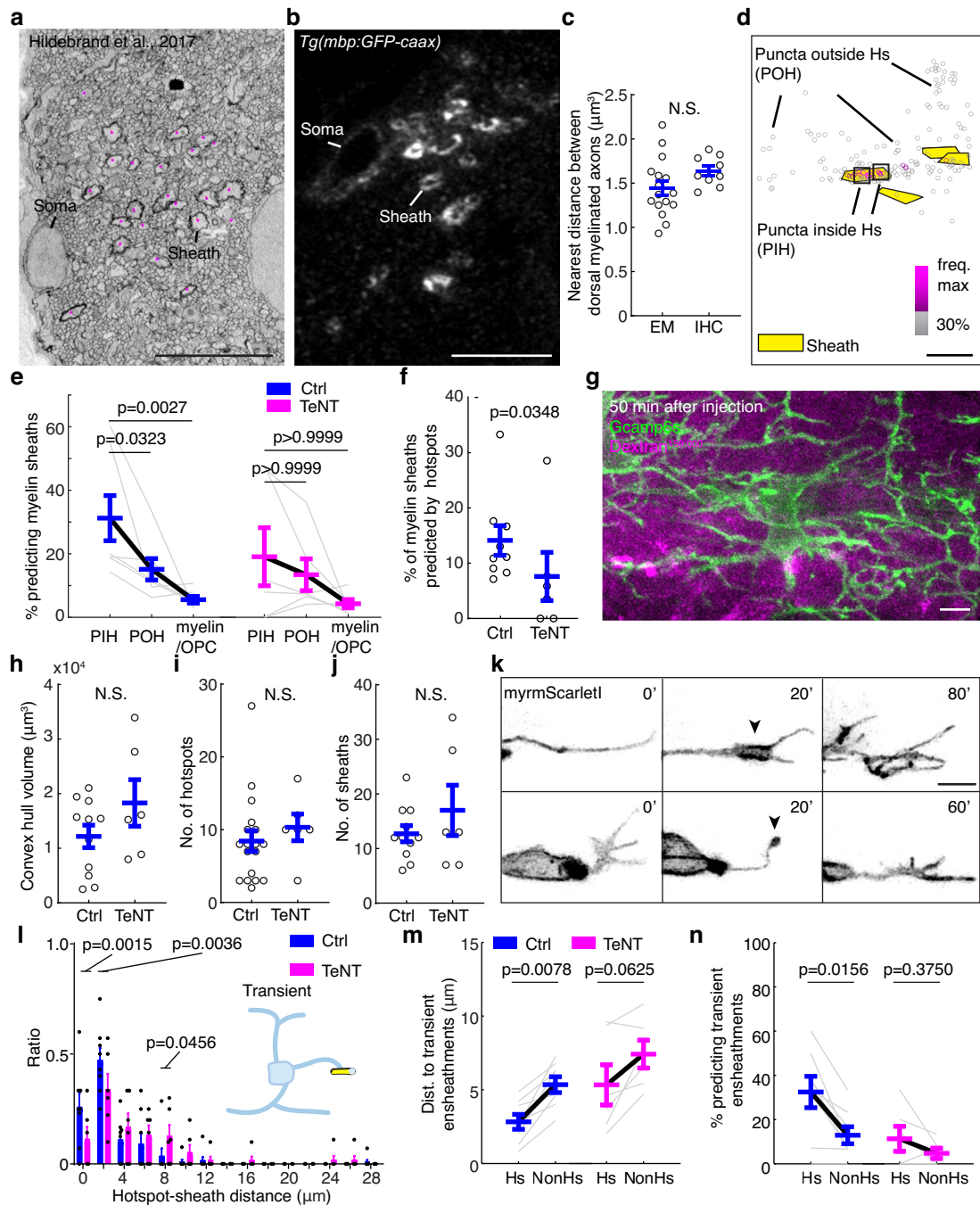
**Extended Data Fig. 2 | MAGUK and Gephyrin puncta numbers in OPCs increase during early development and exhibit small differences across CNS regions.** (a) Quantification of MAGUK (green) and Gephyrin (magenta) puncta number per OPC in the spinal cord at different ages by IHC. From left,  $n = 20, 18, 8, 17, 24,$  and  $8$  cells from at least 6 fish per condition. (b) Quantification of MAGUK (green) and Gephyrin (magenta) puncta number per OPC at 3 dpf across different CNS regions. FB&MB, forebrain and midbrain; HB, hindbrain; SC, spinal cord. From left,  $n = 34, 59, 43, 34, 18,$  and  $40$  cells from at least 10 fish per condition. (c) Schematic model showing the neuron-rich (NR) and axon & synapse rich (AR)

regions and two representative images showing OPCs with soma localized to NR (top) and AR (bottom) regions in *Tg(olig1:Kalta4,10xUAS:myrGFP)* spinal cord. (d) Quantification of MAGUK (green) and Gephyrin (magenta) puncta number per OPCs in NR or AR regions at 2-3 dpf. From left,  $n = 14, 5, 15,$  and  $10$  cells from at least 5 fish per condition. All data are represented as mean  $\pm$  SEM; N.S., not significant (exact  $p$  values are provided in Source Data); (a-b) Kruskal-Wallis test followed by Dunn's multiple comparison test; (d) two-sided Mann-Whitney test; scale bar  $5 \mu\text{m}$ .



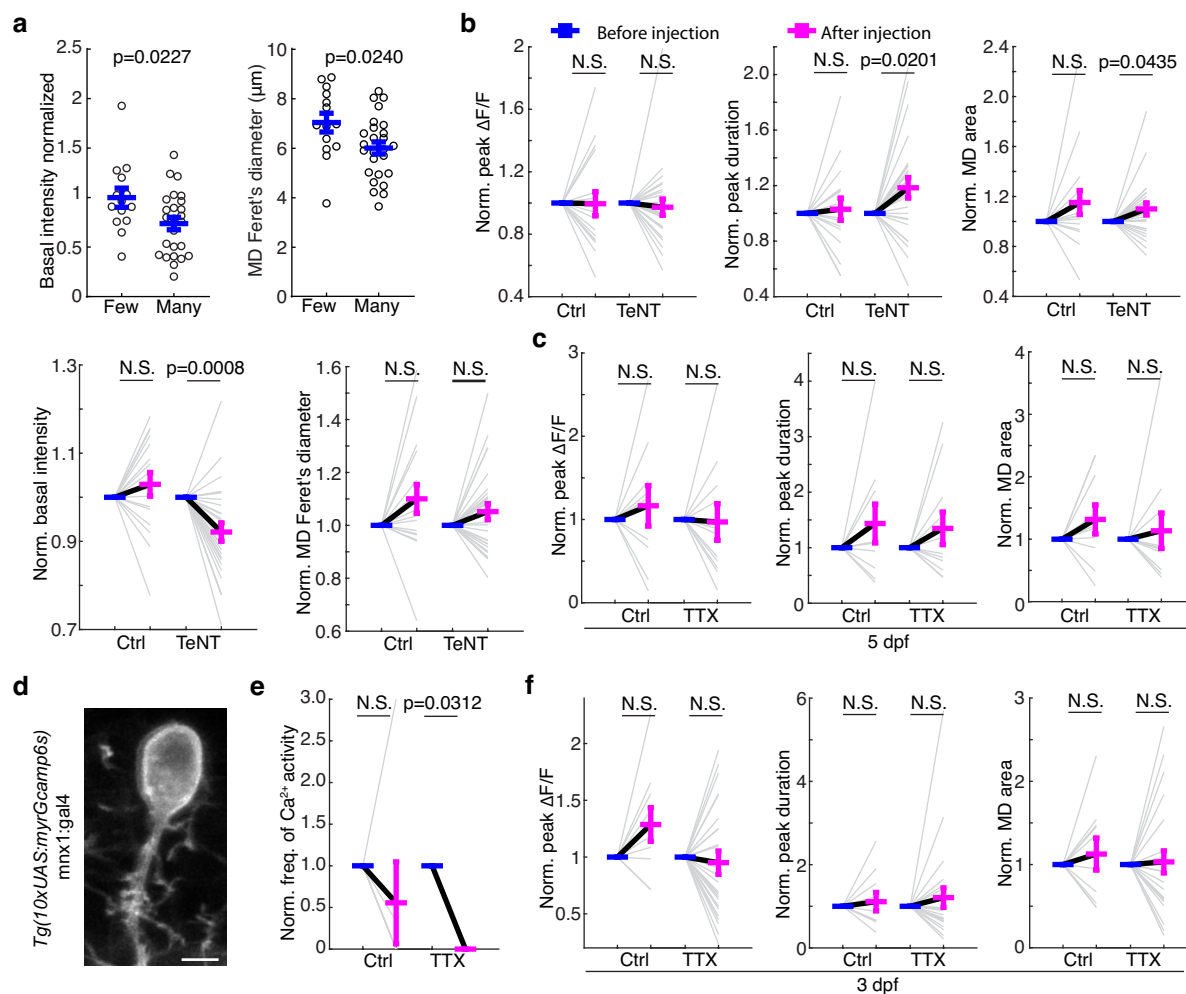
**Extended Data Fig. 3 | *In vivo* characterization of PSD-95-GFP and GFP-gephyrin.** (a) Puncta diameter of PSD-95-GFP (green) and GFP-Gephyrin (magenta) in spinal cord neurons (N) and OPCs from 2-3 dpf larvae. From left,  $n = 10, 11, 15,$  and  $29$  cells from at least 8 fish per condition. (b-c) Representative *in vivo* images of (b) PSD-95-GFP or (c) GFP-Gephyrin and synaptophysin-RFP (syn.) in spinal cord OPCs at 3 dpf. From left, single plane images and an example of puncta in OPCs at single planes with 3D reconstructed regions, the merged channels, the PSD-95-GFP or GFP-Gephyrin channels, and the syn. channel. In the examples, the alignments are indicated with arrowheads. (d) The % of PSD-95-GFP and GFP-gephyrin puncta in an OPC that align with presynaptic synaptophysin-RFP in the spinal cord in (b-c).  $n = 13$  and  $20$  cells from at least 10 fish. (e-f) The correlation analysis of puncta number of (e) PSD-95-GFP and (f) GFP-Gephyrin with the corresponding protein overexpression levels at 3 dpf.

The linear fit extrapolated to zero overexpression level is at puncta number of  $28.6$  and  $22.9$ , respectively. (g) Puncta number of PSD-95-GFP (green) and GFP-Gephyrin (magenta) per OPC in the spinal cord at 2 dpf and 3 dpf. From left,  $n = 16, 18, 29,$  and  $14$  cells from at least 5 fish per condition. (h) Representative IHC images of PSD-95-GFP in spinal cord OPCs at 3 dpf with GFP (green) and MAGUK (magenta) antibodies. Left, merged channels; middle and right, single channels. Arrowheads indicate the GFP puncta that colocalize with MAGUK signals; cyan arrows indicate the diffused GFP that does not colocalize with MAGUK signals. (i) % of GFP signal that colocalizes with MAGUK signals from (h) using Imaris.  $n = 4$  and  $6$  fish per condition. All data are represented as mean  $\pm$  SEM; N.S., not significant (exact p values are provided in Source Data); (a, g) two-sided Mann-Whitney test; (e, f) two-sided Pearson correlation analysis with linear regression; scale bars  $5 \mu\text{m}$ .



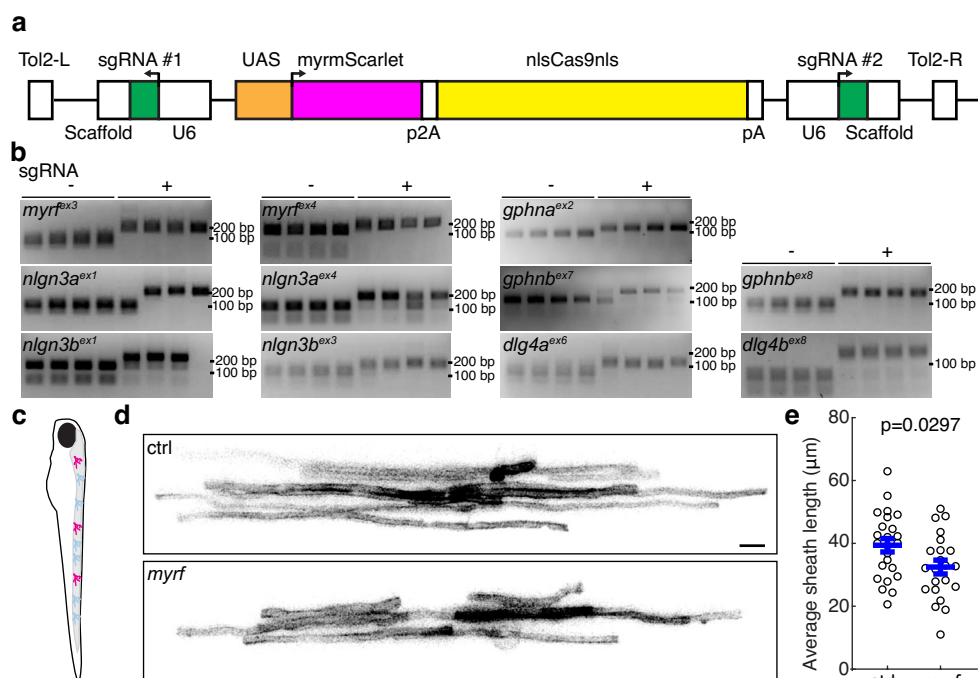
**Extended Data Fig. 4 | Gephyrin hotspots predict a subset of myelin sheath formation in a synaptic release-mediated manner.** (a) EM image of zebrafish spinal cord transverse section at 5 dpf<sup>10</sup>. Magenta dots indicate myelinated axons. (b) IHC images of zebrafish dorsal spinal cord transverse section at 5 dpf in *Tg(mbp:GFP-caax)*. (c) The nearest distance between myelinated axons from (a) and (b). n = 16 and 9 sections from 1 and 6 fish;  $t[23] = 1.627$ . (d) Puncta inside hotspots (PIH) and puncta outside hotspots (POH). (e) Percentage of GFP-Gephyrin PIH and POH that predict future myelin sheaths and percentage of stable sheath volume over OPC volume with control and TeNT treatments. control, n = 8 cells from 7 fish; TeNT, n = 6 cells from 6 fish. (f) Percentage of future stable myelin sheaths predicted by hotspots in OPCs (within 1  $\mu\text{m}$ ). n = 6 cells from 6 fish. (g) Representative image of an OPC after ventricle injection of Dextran<sup>150,000</sup> Antonia Red (magenta). (h-j) Quantification of (h) convex hull volume, (i) hotspot number, and (j) sheath number in control and TeNT

treatment conditions. (h) n = 11 and 6 cells from 10 and 6 fish; (i) n = 18 and 6 cells from 16 and 6 fish; (j) n = 11 and 6 cells from 10 and 6 fish. (k) Representative time-lapse images of transient ensheathments. Arrowheads indicate transient sheaths; minutes. (l) Frequency distribution of hotspot-transient ensheathment distances with control and TeNT treatments.  $F[14, 180] = 23.87$ . control, n = 8 cells from 7 fish; TeNT, n = 6 cells from 6 fish. (m) Quantification of Hs- and nonHs-sheath (stable) distances with control and TeNT treatments. control, n = 8 cells from 7 fish; TeNT, n = 6 cells from 6 fish. (n) Percentage of Hs or nonHs in an OPC that predict where transient ensheathments form with control and TeNT treatments. control, n = 8 cells from 7 fish; TeNT n = 6 cells from 6 fish. All data are represented as mean  $\pm$  SEM; N.S., not significant (exact p values are provided in Source Data); (c) two-sided unpaired *t*-test; (e) Friedman test with Dunn's test; (f, h, i, j) two-sided Mann-Whitney test; (l) Two-way ANOVA and Fisher's LSD test; (m, n) two-sided Wilcoxon matched-pairs signed rank test; scale bars 5  $\mu\text{m}$ .



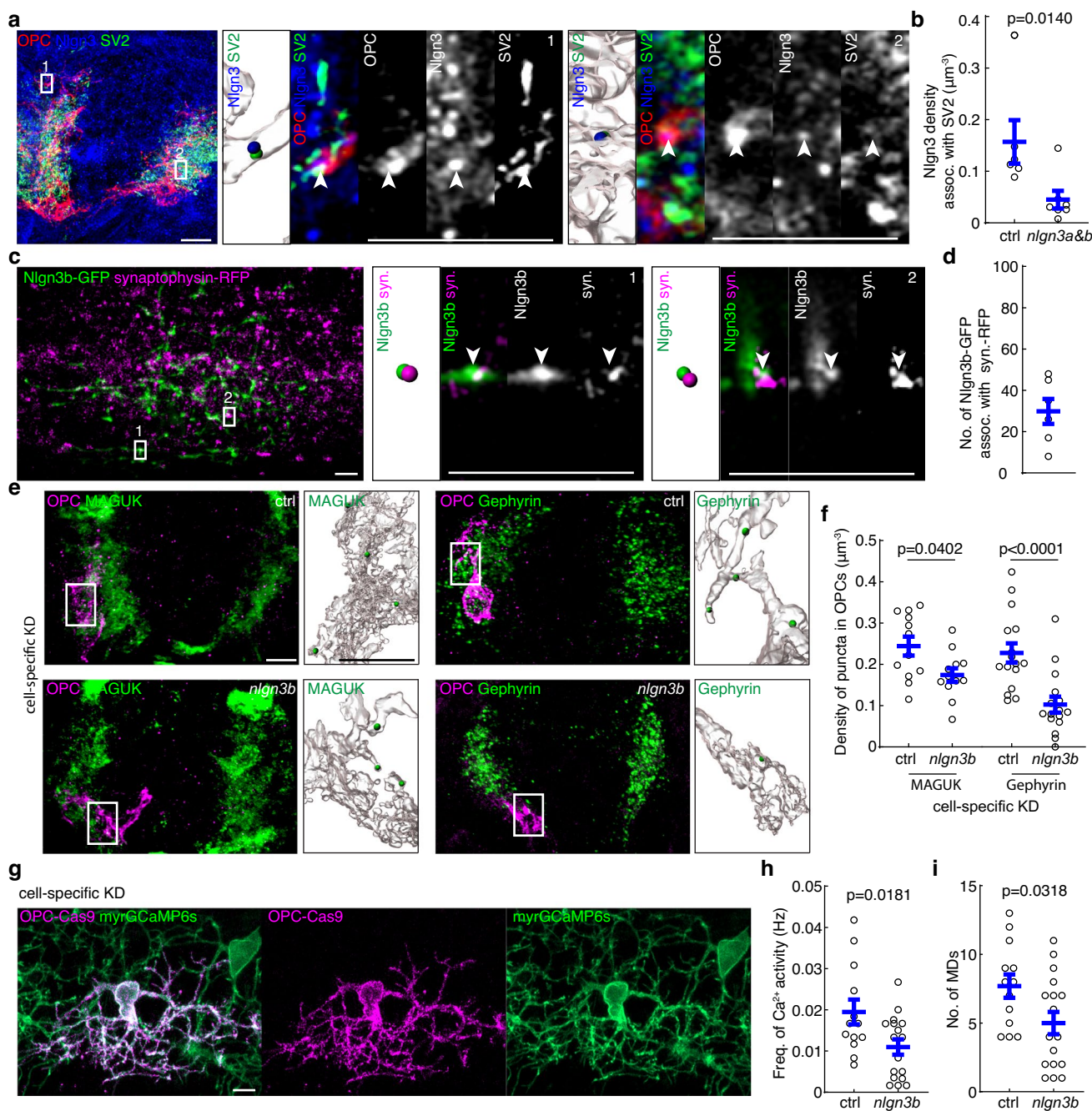
**Extended Data Fig. 5 | The role of synaptic release and neuronal activity in generating OPC  $\text{Ca}^{2+}$  activity.** (a) Basal GCaMP6s intensity and MD feret's diameter in OPCs that neighbor few ( $< 4$ ) and many ( $\geq 4$ ) TeNT1c-expressing axons at 5 dpf. Few,  $n = 14$  cells from 8 fish; many,  $n = 26$  cells from 15 fish;  $t[38] = 2.375$  and  $t[38] = 2.351$ . (b) Normalized peak amplitude, peak duration, area of  $\text{Ca}^{2+}$  MD, basal intensity, and MD Feret's diameter in OPCs before (blue) and after (magenta) injection of control or TeNT solution at 5 dpf. Paired data are indicated with grey lines. Control,  $n = 17$  cells from 13 fish; TeNT,  $n = 26$  cells from 18 fish. (c) Normalized peak amplitude, peak duration, and area of  $\text{Ca}^{2+}$  MD in OPCs before (blue) and after (magenta) injection of control or TTX solution at 5 dpf. Paired data are indicated with grey lines. From left,  $n = 10$  and 11 cells from

6 and 9 fish. (d) Representative images of a primary motor neuron visualized by injecting *mnx1:gal4* into *Tg(10xUAS:myrGCaMP6s)*. (e) Normalized frequency of  $\text{Ca}^{2+}$  activity in motor neurons before (blue) and after (magenta) injection of control or TTX solution at 5 dpf.  $n = 7$  and 6 cells from 5 and 5 fish. (f) Normalized peak amplitude, peak duration, and area of  $\text{Ca}^{2+}$  MD in OPCs before (blue) and after (magenta) injection of control or TTX solution at 3 dpf. Paired data are indicated with grey lines. From left,  $n = 10$  and 24 cells from 7 and 13 fish. All data are represented as mean  $\pm$  SEM; N.S., not significant (exact p values are provided in Source Data); (a) two-sided unpaired  $t$ -test or (b,c,e,f) two-sided Wilcoxon matched-pairs signed rank test; scale bars  $5 \mu\text{m}$ .



**Extended Data Fig. 6 | Cell-specific knockdown system is efficient to disrupt genes in oligodendrocytes in zebrafish.** (a) Schematic of the plasmid (10xUAS:myrmScarlet-p2A-Cas9, U6:sgRNA1;U6:sgRNA2) used to induce cell-specific Cas9 expression with membrane labeling and 2 separate U6-driven sgRNAs. (b) Representative gel images of digested PCR product of genomic regions targeted by the sgRNAs. Each lane represents a single embryo at 1 dpf. The left 4 lanes are uninjected (-) and the right 4 lanes are injected (+) with sgRNAs and Cas9 protein. (c) Schematic of larva with sparsely labeled

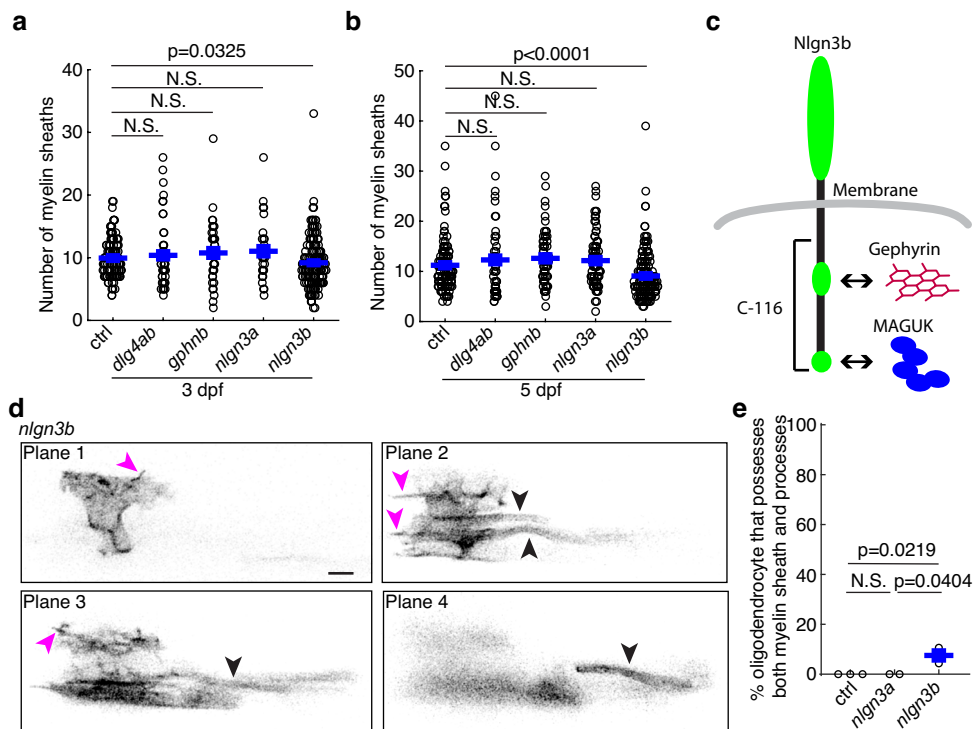
oligodendrocyte lineage cells resulting from *Tg(sox10:Kalta4)* crossed with transgenic fish carrying the plasmid from (a). (d) Representative images of single oligodendrocytes in the spinal cord of *Tg(10xUAS:myrmScarlet-p2A-Cas9, U6:ctrl-sgRNA1;U6:ctrl-sgRNA2)* and *Tg(10xUAS:myrmScarlet-p2A-Cas9, U6:myrf<sup>ex3</sup>-sgRNA;U6:myrf<sup>ex4</sup>-sgRNA)* at 6 dpf. Knockdown of *Myrf* serves as a control for our targeting approach. (e) Average myelin sheath length in (d). n = 24 and 22 cells from 15 fish; t[44] = 2.247. All data are represented as mean ± SEM; (e) two-sided unpaired *t*-test; scale bars 5 μm.



### Extended Data Fig. 7 | Nlgn3 is localized to synapses and knock-down reduces postsynaptic puncta in OPCs.

(a) Representative single-plane IHC images of Nlgn3 (Afi1010<sup>58</sup>) in OPCs with presynaptic marker SV2 in *Tg(olig1:myrScarlet)* spinal cord at 5 dpf. From left, spinal cord sections and two alignment examples with SV2. In each example, from left are 3D reconstructed regions, merged channels, OPC channel, Nlgn3 channel, and SV2 channel. Postsynaptic puncta (blue spheres or arrowheads) and aligned SV2 (green spheres) are indicated. (b) The number of Nlgn3 puncta in an OPC that align with presynaptic SV2 in the spinal cord at 5 dpf from control and F0 larvae with *nlg3a* and *nlg3b* knocked down by sgRNA targeting *nlg3a<sup>ex4</sup>* and *nlg3b<sup>ex1</sup>* and Cas9 protein. From left,  $n = 6$  and  $7$  cells from at least 5 fish each condition. (c) Representative *in vivo* images of Nlgn3b-GFP and synaptophysin-RFP (syn.) in the spinal cord at 5 dpf. From left, single plane image and two examples of puncta in OPCs with 3D reconstructed regions, merged channels, Nlgn3b-GFP channel, and the

syn. channel. The aligned Nlgn3b puncta are indicated with arrowheads. (d) The Number of Nlgn3b-GFP puncta in OPCs that align with synaptophysin-RFP puncta.  $n = 6$  cells from 6 fish. (e) Representative IHC images of MAGUK and Gephyrin in the spinal cord at 3 dpf with ctrl- and *nlg3b*-targeted for cell-specific knockdown. From left, spinal cord sections and 3D-reconstructed images of enlarged regions. In 3D-reconstructed images, only the postsynaptic puncta that fall within OPC process volume are shown (green sphere). (f) Density of MAGUK and Gephyrin puncta in OPCs from (e). From left,  $n = 12, 12, 16,$  and  $16$  cells from at least 8 fish. (g) Representative *in vivo* images of an OPC expressing the cell-specific knockdown construct in *Tg(olig1:Kalta4, olig1:myrGCaMP6s)* at 4 dpf. (h-i) The frequency of (h)  $\text{Ca}^{2+}$  activity and (i) MD number in ctrl- and *nlg3b*-targeted OPCs at 3-4 dpf. ctrl,  $n = 13$  cells from 13 fish; *nlg3b*,  $n = 17$  cells from 16 fish;  $t[28] = 2.260$  and  $t[28] = 2.511$ . All data are represented as mean  $\pm$  SEM; (b,f) two-sided Mann-Whitney test; (h,i) two-sided unpaired *t*-test; scale bars 5  $\mu\text{m}$ .



**Extended Data Fig. 8 | Disruption of *nlgn3b* impairs OPC development and myelination.** (a–b) Number of myelin sheaths per oligodendrocyte in ctrl-, *dlg4ab*-, *gphnb*-, *nlgn3a*-, and *nlgn3b*-targeted oligodendrocytes at (a) 3 dpf and (b) 5 dpf. a, n = 121, 50, 34, 30, and 170 cells from 78, 30, 27, 26, and 97 fish; b, n = 118, 52, 63, 80, and 152 cells from 80, 36, 40, 61, and 93 fish. (c) Schematic showing the domains of Nlgn3b and the region mutated in the dominant-negative construct employed in our studies. (d) 4 single planes of a trapezoid-shaped process in an oligodendrocyte in *nlgn3b*-targeted larvae at 5 dpf. Myelin

sheaths are indicated by black arrowheads and abnormal processes by magenta arrowheads. (e) Percentage of oligodendrocytes that possess both myelin sheath(s) and abnormal processes in ctrl-, *nlgn3a*-, and *nlgn3b*-targeted fish at 5 dpf. n = 119, 84, and 170 cells from 80, 61, and 93 fish, F[6] = 13.52. All data are represented as mean ± SEM; N.S., not significant (exact p values are provided in Source Data); (a, b, e) Kruskal-Wallis test followed by uncorrected Dunn's multiple comparisons test; scale bars 5 μm.

## Reporting Summary

Nature Portfolio wishes to improve the reproducibility of the work that we publish. This form provides structure for consistency and transparency in reporting. For further information on Nature Portfolio policies, see our [Editorial Policies](#) and the [Editorial Policy Checklist](#).

### Statistics

For all statistical analyses, confirm that the following items are present in the figure legend, table legend, main text, or Methods section.

n/a Confirmed

- The exact sample size ( $n$ ) for each experimental group/condition, given as a discrete number and unit of measurement
- A statement on whether measurements were taken from distinct samples or whether the same sample was measured repeatedly
- The statistical test(s) used AND whether they are one- or two-sided  
*Only common tests should be described solely by name; describe more complex techniques in the Methods section.*
- A description of all covariates tested
- A description of any assumptions or corrections, such as tests of normality and adjustment for multiple comparisons
- A full description of the statistical parameters including central tendency (e.g. means) or other basic estimates (e.g. regression coefficient) AND variation (e.g. standard deviation) or associated estimates of uncertainty (e.g. confidence intervals)
- For null hypothesis testing, the test statistic (e.g.  $F$ ,  $t$ ,  $r$ ) with confidence intervals, effect sizes, degrees of freedom and  $P$  value noted  
*Give  $P$  values as exact values whenever suitable.*
- For Bayesian analysis, information on the choice of priors and Markov chain Monte Carlo settings
- For hierarchical and complex designs, identification of the appropriate level for tests and full reporting of outcomes
- Estimates of effect sizes (e.g. Cohen's  $d$ , Pearson's  $r$ ), indicating how they were calculated

*Our web collection on [statistics for biologists](#) contains articles on many of the points above.*

### Software and code

Policy information about [availability of computer code](#)

Data collection

Data analysis

For manuscripts utilizing custom algorithms or software that are central to the research but not yet described in published literature, software must be made available to editors and reviewers. We strongly encourage code deposition in a community repository (e.g. GitHub). See the Nature Portfolio [guidelines for submitting code & software](#) for further information.

## Data

Policy information about [availability of data](#)

All manuscripts must include a [data availability statement](#). This statement should provide the following information, where applicable:

- Accession codes, unique identifiers, or web links for publicly available datasets
- A description of any restrictions on data availability
- For clinical datasets or third party data, please ensure that the statement adheres to our [policy](#)

The animals and experimentally data that support the findings of this study are available from the corresponding authors upon reasonable request.

## Research involving human participants, their data, or biological material

Policy information about studies with [human participants or human data](#). See also policy information about [sex, gender \(identity/presentation\), and sexual orientation](#) and [race, ethnicity and racism](#).

Reporting on sex and gender	N.A.
Reporting on race, ethnicity, or other socially relevant groupings	N.A.
Population characteristics	N.A.
Recruitment	N.A.
Ethics oversight	N.A.

Note that full information on the approval of the study protocol must also be provided in the manuscript.

## Field-specific reporting

Please select the one below that is the best fit for your research. If you are not sure, read the appropriate sections before making your selection.

Life sciences     Behavioural & social sciences     Ecological, evolutionary & environmental sciences

For a reference copy of the document with all sections, see [nature.com/documents/nr-reporting-summary-flat.pdf](https://www.nature.com/documents/nr-reporting-summary-flat.pdf)

## Life sciences study design

All studies must disclose on these points even when the disclosure is negative.

Sample size	No statistical methods were used to pre-determine sample sizes but our sample sizes are similar to those reported in previous publications (Mensch et al., 2015; Marisca et al., 2020)
Data exclusions	No data were excluded.
Replication	All experiments were conducted with different cells, animals and with a minimum of three successful repeats.
Randomization	All animals were randomly chosen from siblings; these animals are then randomly allocated to groups with different treatment; all cells were randomly chosen within the region specified.
Blinding	Data collection was not performed blindly due to the experimental conditions. For example, we injected control and TTX solution into the brain and examine calcium activity afterwards. We tracked each animal and their recording; therefore we are not blind to the treatment. The analysis were performed blindly with "blindr" ( <a href="https://github.com/U8NWXD/blindr">https://github.com/U8NWXD/blindr</a> ).

## Reporting for specific materials, systems and methods

We require information from authors about some types of materials, experimental systems and methods used in many studies. Here, indicate whether each material, system or method listed is relevant to your study. If you are not sure if a list item applies to your research, read the appropriate section before selecting a response.

## Materials &amp; experimental systems

n/a	Included in the study
<input type="checkbox"/>	<input checked="" type="checkbox"/> Antibodies
<input checked="" type="checkbox"/>	<input type="checkbox"/> Eukaryotic cell lines
<input checked="" type="checkbox"/>	<input type="checkbox"/> Palaeontology and archaeology
<input type="checkbox"/>	<input checked="" type="checkbox"/> Animals and other organisms
<input checked="" type="checkbox"/>	<input type="checkbox"/> Clinical data
<input checked="" type="checkbox"/>	<input type="checkbox"/> Dual use research of concern
<input checked="" type="checkbox"/>	<input type="checkbox"/> Plants

## Methods

n/a	Included in the study
<input checked="" type="checkbox"/>	<input type="checkbox"/> ChIP-seq
<input checked="" type="checkbox"/>	<input type="checkbox"/> Flow cytometry
<input checked="" type="checkbox"/>	<input type="checkbox"/> MRI-based neuroimaging

## Antibodies

## Antibodies used

Primary antibodies: chicken anti-GFP (Invitrogen A10262), 1:1000, mouse anti-Pan-MAGUK (NeuroMab K28/86) 1:500, mouse anti-Gephyrin (Synaptic Systems 147011) 1:1000, rabbit anti-Synapsin 1/2 (Synaptic Systems 106002) 1:1000, mouse anti PSD-95 6G6-1C9 (MAB1596) 1:1000, rabbit anti-Glycine receptor (Synaptic Systems 146008) 1:1000, mouse anti-SV2 (DSHB AB\_2315387) 1:1000, rabbit anti-Nlgn3 (nittobo medical Af1010) 1:1000. Secondary antibodies (1:1000): A488 anti-chicken (A11039, Thermo Fisher), A594 anti-rabbit (A32740, Thermo Fisher), A647 anti-mouse IgG1 (115-605-205, Jackson), A647 anti-mouse (A32728, Thermo Fisher).

## Validation

chicken anti-GFP has been verified by the producer (<https://www.thermofisher.com/antibody/product/GFP-Antibody-Polyclonal/A10262>). In addition, we saw no staining outside of the cells expressing GFP.  
 mouse anti-Pan-MAGUK has been verified by the producer ([https://neuromab.ucdavis.edu/datasheet/K28\\_86.pdf](https://neuromab.ucdavis.edu/datasheet/K28_86.pdf)).  
 mouse anti-Gephyrin has been verified by the producer (<https://sysy.com/product/147011>) and further verified by us in zebrafish.  
 Synapsin antibody has been verified by the producer (<https://sysy.com/product/106002>).  
 PSD-95 antibody has been verified by the producer ([https://www.emdmillipore.com/US/en/product/Anti-Post-Synaptic-Density-Protein-95-Antibody-clone-6G6-1C9,MM\\_NF-MAB1596](https://www.emdmillipore.com/US/en/product/Anti-Post-Synaptic-Density-Protein-95-Antibody-clone-6G6-1C9,MM_NF-MAB1596)).  
 Glycine receptor antibody has been verified by the producer (<https://sysy.com/product/146008>)  
 SV2 antibody has been verified by the producer (<https://dshb.biology.uiowa.edu/SV2>)  
 Nlgn3 antibody has been verified by the producer (<https://nittobo-nmd.co.jp/pdf/reagents/Nlgn3.pdf>) and further verified by us in zebrafish.  
 In addition, the synaptic proteins antibody staining shows signal only in the same axon rich regions of the spinal cord in our hands.

## Animals and other research organisms

Policy information about [studies involving animals](#); [ARRIVE guidelines](#) recommended for reporting animal research, and [Sex and Gender in Research](#)

## Laboratory animals

Zebrafish: nacre, AB and transgenic lines (based on nacre or AB) were used. Male and female fish of 3 to 12 months-old were mated; larvae fish of 2 dpf to 5 dpf were used for experiments.  
 Transgenic zebrafish lines and strains from previous studies: Tg(sox10:Kalta4) (Almeida et al., 2015), Tg(olig1:Kalta4) (Marisca et al., 2020), Tg(huc:synaptophysin-RFP) (Marisca et al., 2020), Tg(olig2:dsRed), Tg(sox10:GFP-caax). The following lines were newly generated for this study: Tg(10xUAS:myrGCaMP6s), Tg(olig1:myrGCaMP6s), Tg(10xUAS:myrGFP), Tg(10xUAS:myrmScarlet), Tg(olig1:myrmScarlet).

## Wild animals

Not used.

## Reporting on sex

sex were not determined at this age when we carried out experiments.

## Field-collected samples

Not used.

## Ethics oversight

All zebrafish experiments and procedures were performed in compliance with institutional ethical regulations for animal testing and research at Oregon Health and Science University (OHSU). Experiments were approved by the Institutional Animal Care and Use Committee of OHSU.

Note that full information on the approval of the study protocol must also be provided in the manuscript.